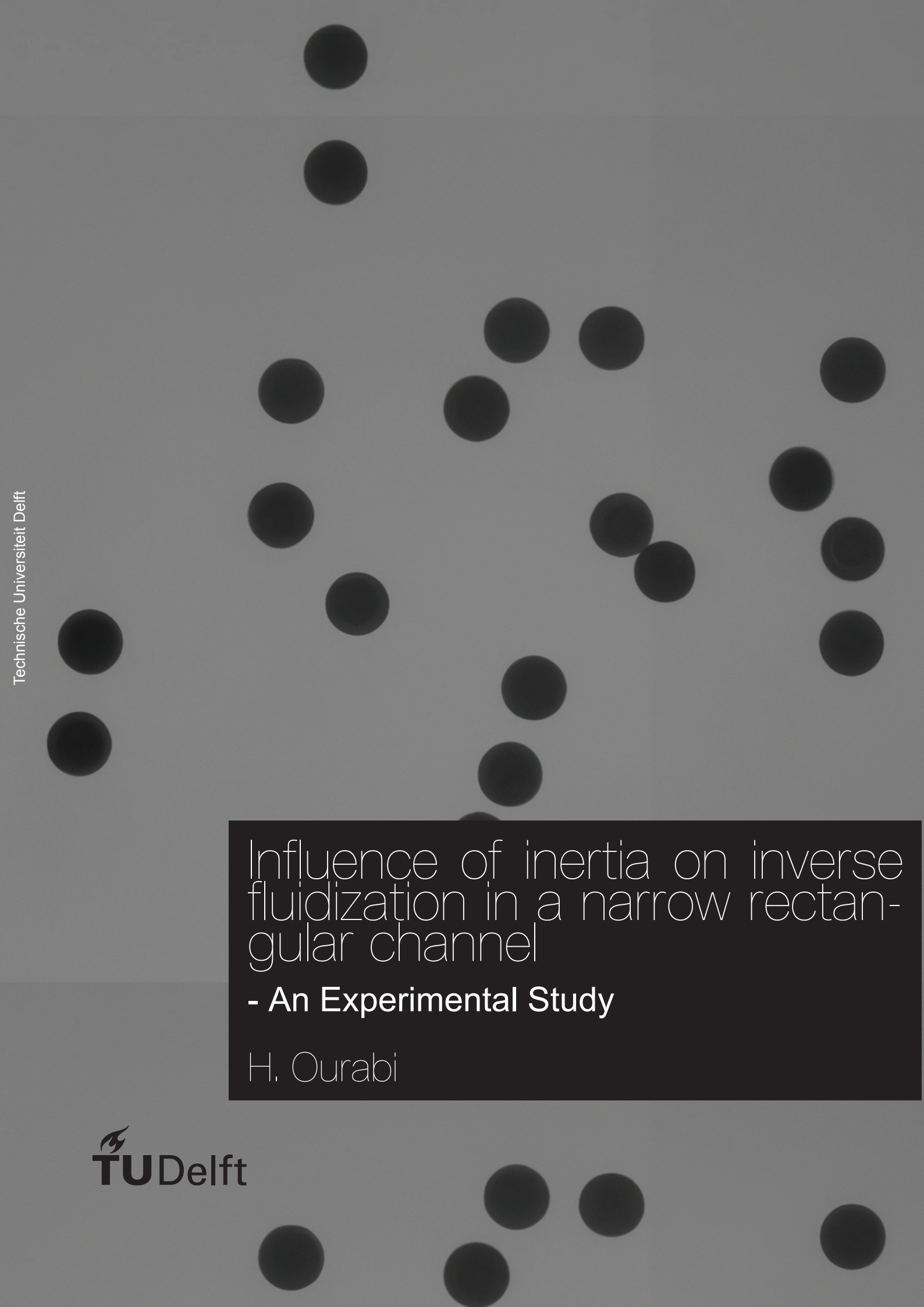

Technische Universiteit Delft

Influence of inertia on inverse fluidization in a narrow rectangular channel

- An Experimental Study

H. Ourabi

TU Delft

Influence of inertia on inverse fluidization in a narrow rectangular channel

by

H. Ourabi

to obtain the degree of Master of Science
at the Delft University of Technology,
to be defended publicly on Tuesday August 29, 2023 at 10:00 AM.

Student number:	5476097	
Project duration:	November, 2022 – August, 2023	
Thesis committee:	Dr. ir. W.-P. Breugem,	TU Delft, supervisor
	Dr. ir. W. Hogendoorn,	TU Delft, co-supervisor
	Dr. ir. T.M.J. Nijssen,	TU Delft

An electronic version of this thesis is available at http://repository.tudelft.nl/.

TU Delft

Preface

This thesis marks the fulfilment of the required number of credits to be obtained for the Masters in Mechanical Engineering program under the track 'Energy, flow, and process technology' at the Delft University of Technology. The experimental setup was built in the Laboratory of Aero- and Hydrodynamics, Department of Process and Energy under the supervision of Dr.ir. Wim-Paul Breugem and co-supervision of Dr.ir. Willian Hogendoorn. The work in this thesis focused on the design of an experimental setup and the development of image processing tools. The main goal was to study the effect of inertia and bulk solid volume concentration on the microstructure of fluidized suspensions. This report aims to provide a detailed documentation of the entire experimental campaign and discusses the results obtained thereof.
Constructive criticisms on the structure presentation of the report are welcome and I take responsibility for any flaw or loss of clarity in the report. Criticisms on any conceptual/logical flaw in the report is also welcome as I am ready to unlearn and relearn. The particle tracking velocimetry (PTV) code developed for this project can be found in the bibliography. The data corresponding to the plots in the report can be obtained upon request.

Hamza Ourabi
Delft, August 2023

Acknowledgements

When I first arrived at TU Delft, I felt like the smartest person, but the more people I met, the more humbled I became. Here's to the first time I failed a course. Here's to failing every single course during my first quarter at TU Delft. Here's to the meniscus injury and surgery I had during my first week in Delft. Here's to building an experimental setup from scratch and everything that comes with it. The frustration when something went wrong without having any idea why, and the joy when the first 3 spheres got fluidized. And here's to all the hardships I had to endure to become a better version of myself. I would have never been able to get through all of that alone. This section is dedicated to everyone who helped me reach this point by making life easier or, at times, more challenging.

I'd like to start by thanking my supervisors to whom I owe this research. Dr. Wim-Paul Breugem and Dr. Willian Hogendoorn, thank you for all the critical and valuable comments throughout this thesis project. Your guidance has helped me develop as a person and a researcher. You have always ensured the best outcome from this research and made sure I understood whatever I was doing. You've taught me to focus more on quality over quantity, and you've been patient with me despite my occasional sloppiness during our biweekly meetings. You've spent hours explaining various topics, whether it was about building the setup or understanding the physics behind the problem. I would also like to thank Dr. Tim Nijssen for agreeing to be a part of the graduation committee.

I'd like to personally thank Rein van den Oever, Edwin Overmars, Martijn Karsten, Bart Hoek, and Michel van den Brink for helping me build the experimental setup. They provided me with the necessary optical devices, helped connect the sensors, and offered insightful ideas while constructing the setup, such as placing the chiller on top of the cabinet. They consistently provided us with the required laboratory equipment.

This journey wouldn't have been possible without everyone I met during my high school and bachelor's years. To my teachers, professors, friends, and colleagues, I want to express my gratitude. I'd like to thank the Malakies for being there at P&E, and all the other great people I have met at 3mE. It has been a pleasure to be part of MSA Ibn Finas, I have enjoyed every activity that we have organized.

The person I am today is a result of everyone back home in Syria and Egypt. To all my friends back in Egypt who made every minute count during the brief week I would go back home and who continue to support me. Most importantly, both my parents and my siblings for their unwavering support throughout my university years. It's been a long 6 years away from home, and I've missed many special occasions. You have encouraged and supported me with every decision that I have made. Finally, I'd like to thank my uncle Abdulrahman and his family for making me feel at home here in the Netherlands. Family isn't just important; it's everything.

Abstract

The presence of particles in a flow can change the flow behaviour in an unpredictable manner, that leads us to multiphase flow. Multiphase flows are present in nature and in everyday life around us. The most common example of a multiphase flow, that one can think of, is the treatment of drinking water using liquid-solid fluidization in softening processes. Multiphase flows can also have very high relevance in various practical applications ranging from sedimentation of particles for process industries, transport of a dense suspension (slurry) through a pipe and dredging applications for land reclamation. Even though a lot of research has been done on liquid-solid fluidization in inertial and viscous dominated regimes, it remains far from being understood completely.

Experimental studies were conducted on the fluidization of monodisperse solid spheres within a rectangular channel. This research saw the development of an experimental setup, to study this phenomenon. The bulk solid volume fraction was studied in three different regimes. At a dilute regime ($\Phi \leq 4\%$), moderate regime ($\Phi = 8 - 14\%$), and a dense regime ($\Phi \geq 15\%$). To study the impact of inertia, three distinct Galileo numbers in the inertial regime were examined: Ga = 147, 196, and 252. At these values, a singular settling/rising sphere presents markedly varied wake and path characteristics. Throughout the study, the particle/fluid mass density ratio remained constant at 0.87. Results indicate that within the range of $\Phi = 4 - 18\%$, both the microstructure and dynamics of the suspension are heavily influenced by the bulk solid volume fraction. This aligns qualitatively with previous literature.

Enhanced fluidization was noticed in the experiments. This is usually driven by the formation of clusters. Particle clustering within these regimes is driven by various mechanisms: trapping of particles in wakes, a drafting–kissing–tumbling (DKT) instability causing vertically aligned particles to swiftly realign horizontally, and multiparticle interactions with collisions playing a minor role. On the macrostructure level, intrinsic convection was captured in the fluidization column. To further study these characteristics, instantaneous snapshots were illustrated for varying cases. Profiles for both mean velocity and root-mean-square (RMS) velocity were obtained. Wall effects emerged as pronounced, diminishing in importance with increased bulk solid volume fraction and augmented Ga values. Intrinsic convection is observed in these experiments, and the velocity profiles provided an indication. Probability density functions (pdf) for normalized velocities highlighted evident particle clustering.

Contents

List of Figures

1

Introduction

Fluidization and sedimentation play an integral role in diverse domains, encompassing chemical engineering, environmental engineering, and wastewater management. Fluidization imparts a fluid-like behavior to solid materials, causing enhanced mixing and better heat and mass transfer. This enhancement facilitates process efficiency and productivity rates. Recently, these processes have gained attention in various fields including biotechnology, food processing, and pharmaceuticals [1].
In the Netherlands, the employment of liquid-solid fluidization is prevalent in land reclamation and treatment processes of drinking water [2]. The insights gleaned from fluidization and sedimentation experiments serve as valuable assets in the optimization of industrial systems design and operation. These systems include chemical reactors for the synthesis of petrochemicals [3], and environmental engineering frameworks particularly in the context of land reclamation and dredging applications [4].

In addition, fluidization is employed in mining ventures to augment the retrieval of precious minerals through enhanced separation of the target minerals from extraneous materials [5]. This yields performance improvements and sparks innovation in the domain. Figure 1.1 illustrates instances where fluidization and sedimentation are fundamental components of these sectors.

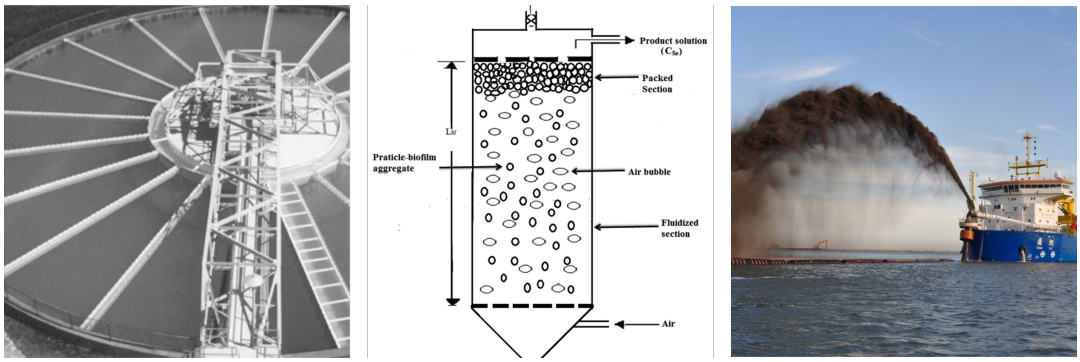

Figure 1.1: Clarifier for Biological Phosphorus Removal [6]; Diagram of a Semi-fluidized Biofilm Reactor in Three-phase Operation [7]; Trailing Suction Hopper Dredger 'Tongyuan' Engaged in Operation [8].

This research aims to show the complications in sedimentation and fluidization processes through experiments. In practical terms, this encompasses an investigation into the various flow regimes at play at different levels of inertial effects. This was achieved by changing Galileo number, as well as the bulk solid volume fraction. Experiments focusing on the inverse fluidization of light spheres were conducted in a rectangular channel. This channel is equipped with direct optical access, facilitating the tracking of spheres to study the microstructure formations using a high-speed camera.

This thesis starts with an overview of the underlying theory and important fluid parameters characterizing the flow for the processing of experimental data in Chapter 1.1. This is followed by a comprehensive review of previous literature in Chapter 1.2. Subsequently, the goals and motivation behind this research are shown in Chapter 1.3. Chapter 2 sheds light on the experimental methodology. Starting with the details of the experimental setup and apparatus employed in Chapter 2.1. Followed by collecting data using a data acquisition system. The camera calibration is then discussed. Additionally, the experimental procedure is explained, with the necessary steps needed to run an experiment. Chapter 2 also shows an overview of the data processing, wherein the particle tracking velocimetry technique was developed for results analysis. The crucial procedure behind data processing is also addressed. Chapter 3 delves into the results and outcomes, presenting the main findings of this research. Chapter 4 includes the final conclusions and discussion. Finally, Chapter 5 discusses recommendations for future work regarding the relevance of inertia in the microstructure of fluidized suspensions.

1.1. Theory and Relevant Parameters

The physical phenomenon of fluidization of monodisperse non-colloidal spherical particles can be characterized using four primary dimensionless numbers. The first of these is the Galileo Number (Ga), which is a measure of the relative strength of buoyancy and viscous forces. At a viscous-dominated regime, $Ga < O(1)$, the effect of inertia is negligible and that is referred to as the Stokes regime. Inertial effects become significant for $Ga > O(1)$ and increasingly dominate as Ga increases. It is used to evaluate the inertial effects in the fluid phase for a single settling particle. The settling or rising speed of particles is primarily determined by the Galileo number. Secondly, for the mass density ratio ($\overline{\rho}$) is used to assess the relative importance of particles with respect to fluid inertia. It affects the particle response time through path instabilities. This may affect the settling/rising speed of particles but only when the particles are very light ($\overline{\rho} \leq 0.3$) [9]. The third dimensionless number is the particle volume concentration (Φ), which represents the proportion of solid particles in the fluid and can impact the drag coefficient of the particle. Φ is a measure of the relative importance of particle-particle interactions, as well as the mean free path between particles. Finally, the ratio of the particle diameter to the system length scale (D_p/L) is used to study the effect of confinement. Confinement becomes important when the flow is affected by the nearby walls.

To apply the following dimensionless numbers and for correct characterization of the problem. The particles are assumed to be fully rigid, non-colloidal, spherical, and monodisperse. Starting with the Galileo number, it is defined as follows:

$$Ga = \sqrt{\frac{(\rho_p - \rho_f) g D_p^3}{\rho_f \nu_f^2}}, \tag{1.1}$$

where ρ_p and ρ_f are the densities of solid particles and working fluid respectively, g is the gravitational acceleration, D_p is the diameter of the spherical particles, and ν_f is the kinematic viscosity of the working fluid. Assuming a drag coefficient, C_d is O(1), the characteristic velocity scale is given by $U_{char} = \sqrt{\mid \rho_p - \rho_f \mid gd/\rho_f}$ and D_{char} is the particle's diameter. The Galileo number is a proxy of the Reynolds number and can be written in this form, $Ga = Re = U_{char} D_{char}/\nu_f$.

The mass density ratio is defined as follows:

$$\overline{\rho} = \frac{\rho_p}{\rho_f}. \tag{1.2}$$

The mass density ratio is of relative importance when the particle undergoes an acceleration or deceleration and/or the wake behind the particle becomes unsteady. Otherwise, the fall/rise velocity is solely determined by the Galileo number. The mass density ratio in the present experiments is smaller than 1, ($\overline{\rho} \leq 1$), indicating the particles are lighter than the working fluid.

The hydrodynamic interactions as well as direct collisions depend mainly on the bulk solid volume fraction. The solid volume fraction is defined as follows:

$$\Phi = \frac{m}{\rho_p h_{bed} A}, \tag{1.3}$$

where m is the total mass of the solid particles used, A corresponds to the cross-sectional area of the fluidized bed, and h_{bed} is the height over which the particles are suspended. The solid volume fraction is important when particle spacing is equivalent to particle size. For a reference particle, this results in a flow pattern that is significantly altered from that in an unbounded fluid as the flow passage becomes meandering.

A proper understanding of fluidization requires the study of the forces acting on a single rising or settling spherical particle in a liquid domain. For a light spherical particle that has the tendency to rise but is pushed in the downwards direction as shown in Figure 1.2. A drag force is acting in the downwards direction while the net buoyancy force is acting in the upwards direction. The forces acting on a single spherical particle are defined as follows:

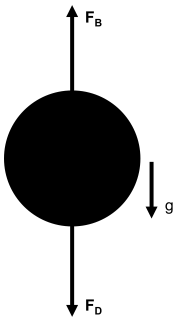

Figure 1.2: Force balance on a single rising sphere in a fluid medium.

$$F_g = \frac{4\pi}{3}\left(\frac{D_p}{2}\right)^3 g(\rho_p - \rho_{mix}), \tag{1.4}$$

$$F_d = \frac{1}{2}C_d\rho_f U_{t,\infty}^2 \pi\left(\frac{D_p}{2}\right)^2, \tag{1.5}$$

where ρ_{mix} is the mixture's density calculated as follows:

$$\rho_{mix} = \Phi\rho_p + (1-\Phi)\rho_f. \tag{1.6}$$

Additionally, a two-fluid model approach was used to estimate the fluid continuity equation for a (statistically) homogeneous and steady flow as follows:

$$(1-\Phi)\langle u_f\rangle^f = C1, \tag{1.7}$$

where $\langle u_f\rangle^f$ is the intrinsic fluid velocity, and $C1$ is a constant corresponding to the fluidization velocity. Based on a similar approach, the conservation of momentum reduces to:

$$0 = -\frac{\partial\langle p_f\rangle^f}{\partial z} + \rho_f g + \Phi(\rho_p - \rho_f)g. \tag{1.8}$$

The pressure drop in the momentum equation balances the net weight of the liquid and immersed solid particles per unit volume. The first term in this equation calculates the total pressure drop over the fluidization column. The second term in Eq. (1.7) represents the hydrostatic pressure drop in the fluidization column. The last term in Eq. (1.7) represents the contribution from dynamic pressure drop related to the fluidization of the particles. When the fluidization is too low and particles are not fluidized (i.e., particles are contained in a packed bed), the dynamic pressure drop increases with the fluidization velocity until the minimum fluidization is reached at which particles become mobile. Then a constant pressure drop is reached which indicates a fully fluidized bed.

Either Richardson and Zaki's [10] or Ergun models [11] can be used to predict the pressure drop over unit length. The developed R-Z empirical formula that predicts the suspension's velocity as a function of the solid volume fraction and an experimentally determined exponent n is presented in this section. Most studies fitted their experimental results by modifying the exponent n in terms of Reynolds number based on terminal velocity and wall effects (d/L). However, based on different experiments, the exponent n can be modified to further account for wall effects. The empirical correlation given by R-Z is given by:

$$\frac{\langle u_f\rangle}{U_i} = (1-\Phi)^n, \tag{1.9}$$

where $\langle u_f\rangle$ is the superficial fluidization velocity, U_i is the superficial fluid velocity at $\Phi = 0$. Richardson [10] calculated U_i using the following equation:

$$U_i = U_{t,\infty} \cdot 10^{-D_p/L}, \tag{1.10}$$

where $U_{t,\infty}$ is the particle's terminal velocity in free space and calculated as follows:

$$U_{t,\infty} = \sqrt{\frac{4(\rho_p - \rho_f) g D_p}{3\rho_f C_d}}. \tag{1.11}$$

Exponent n is determined based on the particle terminal Reynolds number $Re_t = \rho_f U_{t,\infty} d/\mu_f$, there is a wide range to calculate n, two of them are given as follows:

$$\begin{aligned} n &= \left(4.4 + 18\frac{D_p}{L}\right) \cdot Re_t^{-0.1} \qquad \text{for} \quad 1 \le Re_t \le 200\cdot \\ n &= 4.4 \cdot Re_t^{-0.1} \qquad \text{for} \quad 200 \le Re_t \le 500\cdot \end{aligned} \tag{1.12}$$

Richardson and Zaki's correlation accounts for the flow field around a particle that is disturbed by the nearby presence of other particles, causing hindered fluidization. Yin and Koch [12] suggested that R-Z is only valid when clustering is not present and suggested a relation of clustering to inertia which most likely depends on Ga and Φ. In principle, that could have been accounted for by the empirical correlation, but it turns out that when clustering plays a role, the actual required fluidization velocity deviates from the power-law behavior.

As the solid volume fraction increases, collisions between particles become more relevant as well as lubrication and collision dynamics. The lubrication force has more influence in Stokes regime. When the Galileo number and the solid volume fraction increase, the collisions will have significant effects on the particles. To know whether these collisions shall be studied or not, the impact Stokes number is calculated which is the ratio of initial particle momentum to the loss by viscous lubrication force.

$$St_{impact} = \frac{\rho_p V_p u_{rel}}{\frac{3}{2}\pi\mu_f D_p^2}, \tag{1.13}$$

where V_p is the volume of the particle, and u_{rel} is the particle's relative velocity. u_{rel} is estimated based on the statistically averaged velocities of each particle which scales with the same order of magnitude of the superficial fluidization velocity. For St_{impact} smaller than O(10), the particle does not rebound therefore all the kinetic energy is dissipated by the lubrication force prior to collision. To compute St_{impact}, the RMS velocity is needed that scales with the fluidization velocity. The typical distance between the particles and the wall is measured. Finally, the trajectory of a single particle for the mean free path is needed to obtain a pair distribution function.

To estimate the pressure loss due to the wall effects in a single-phase flow, the Reynolds number is calculated to estimate a skin friction loss coefficient for a rectangular duct flow. Reynolds number is calculated as follows:

$$Re = \frac{U D_H}{\nu}, \tag{1.14}$$

where D_H is the hydraulic diameter of the duct relating the area to the perimeter as $D_H = 4A/P$. To further account for the solid phase in the fluidization column, the mixture Reynolds number is calculated as follows:

$$Re_{mixture} = \frac{\rho_f \langle u_f \rangle^f D_H}{\mu_{eff}}, \tag{1.15}$$

where μ_{eff} is the effective viscosity which is calculated based on Maron-Pierce [13] viscosity model defined below:

$$\frac{\mu_{eff}}{\mu_f} = \left(1 - \frac{\Phi}{\Phi_{max}}\right)^{-2}, \tag{1.16}$$

where Φ_{max} is the maximum solid volume fraction for a fluidized bed.
Based on these values, the Reynolds number can be calculated, and the Darcy-Weisbach friction factor f_f is obtained (see Chapter 3.1). After obtaining f_f, the pressure drop over the length is estimated as shown:

$$\frac{\Delta P}{L} = f_f \frac{\rho_f}{2} \frac{(\langle u_f \rangle^f)^2}{D_H} \tag{1.17}$$

The pressure drop due to the wall friction has a significant influence. In chapter 3.1, a moody diagram is obtained that shows the pressure drop in the channel at different Re.

1.2. Review of previous literature

To cover some of the most influential work done on fluidization and sedimentation, this section has been divided into several subsections showing the current state of the art in each. Firstly, starting with previous literature on a single freely moving sphere. Followed by that is fluidization and sedimentation of dilute suspensions. Inverse fluidization is then considered in this section, where light spheres are used. Finally, liquid-solid fluidization in a narrow rectangular channel is presented. A regime map is added that includes previous experimental work done, and identifying a research gap where no previous studies have been performed before.

1.2.1. Freely moving sphere

Fluidization and sedimentation experiments have been extensively studied since the development of Stokes' correlation in 1856 for forces on a single particle in an infinite viscous fluid [14]. The effect of gravity on collective particle sedimentation was investigated by Cloe and Clevenger [15], followed by Robinson's study of factors affecting sedimentation [16]. With the tremendous development in the chemical engineering industry, numerous studies were conducted to understand the transport phenomena in fluidization.

Experiments on a single sphere rising or settling freely have been conducted, which are independent of solid volume fraction. The density ratio can be fixed, either smaller than 1 for light spheres, or larger than 1 for heavy spheres. If experiments are performed in a large tank, the confinement effect is reduced and might be negligible. Other studies have also been done to investigate the wall effect the terminal velocity and path trajectories of a single particle [17, 18]. These are further explained in section 1.2.4.

Focusing on the effect of Ga on the path and wake trajectories, recent studies have shown that inertia becomes important even at Galileo numbers close to 1 [17, 19]. These effects introduce different instabilities at different solid volume fractions and anisotropy in the microstructure. Recently, Shravan et al. [9] studied the path characteristics of a single sphere for a wide range of Galileo numbers ($Ga = 100 - 700$). Increasing the Galileo number led to various path instabilities, resulting in different path characteristics such as steady oblique, oscillating oblique, high-frequency oscillating, chaotic, and zigzagging motion as shown in Figure 1.3 [20]. These characteristics are independent of particle volume concentration and are only affected by the Galileo number and density ratio. The benefits of conducting such experiments are that they provide insight into the behavior of a single freely moving sphere, which exhibits a variety of path and wake instabilities.

Considering all the different path and wake trajectories present for a single rising/settling sphere makes the problem harder. Thus, it is worth noting that the wake trajectories present for a single moving sphere induce the question of how these trajectories would be affected by particle-particle interactions. Consequently, it is essential to investigate multiple spheres' behavior to provide insight into the collective particle dynamics.

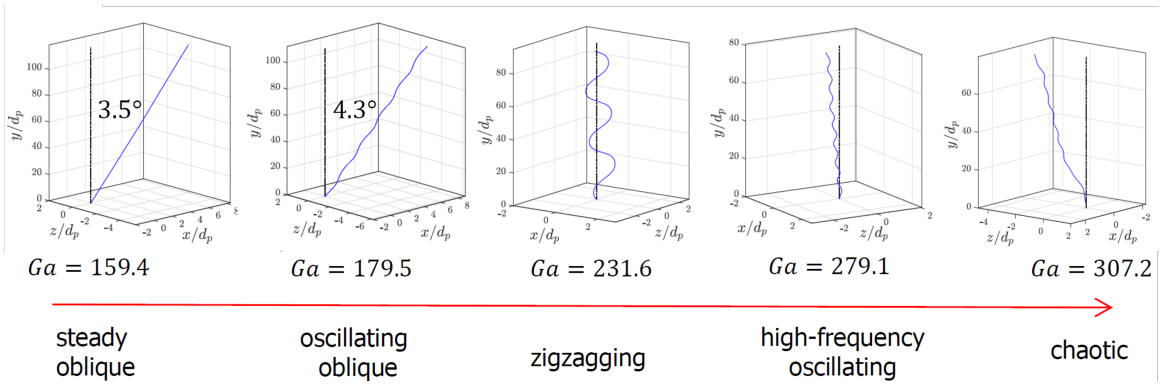

Figure 1.3: Different trajectories present at increasing Ga for polypropylene spheres at $\overline{\rho} \approx 0.87$. Reproduced from [9].

1.2.2. Fluidization and sedimentation

In many industrial processes, the processes of fluidization and sedimentation are interrelated. The forces acting on particles in sedimentation are similar to those acting on the particles being fluidized [21]. The correlations obtained can be used interchangeably [22]. Although fluidization and sedimentation are considered dynamically similar, this is not entirely accurate in the case of confinement. The relative velocity of spheres in fluidization differs from that in sedimentation. In fluidization, a no-slip boundary condition exists at the walls, resulting in zero velocity.

Experiments on fluidization and sedimentation started with Wilhelm and Kwauk in 1948 [23], where they initially observed particle clusters in fluidized beds, followed by Kaye and Boardman in 1962 [24], who demonstrated the importance of particle-particle interactions, even for dilute suspensions, bulk solid volume fraction, ($\Phi \leq 0.05\%$). One of the most extensive experimental investigations was published in 1954 by Richardson and Zaki [22]. For suspensions of spheres, the authors found that the sedimentation velocity of a suspension can be modeled empirically as the product of the terminal velocity of a single settling particle and a hindered settling function given as a power law in the bulk voidage fraction. This formula is accurate for different flow regimes at different solid volume fractions, but clustering effects were not considered in the formula.

Richardson and Zaki consistently found that the settling velocity of dense suspensions is always smaller than the settling velocity of a single sphere. Yin and Koch [12] suggested that RZ is only valid when clustering is not present. They have attributed the anisotropy (clustering) and deviation from the power-law behavior to inertial effects such as drafting, kissing, and tumbling (DKT). DKT was first noticed by Fortes et al. [25] in their experimental studies. Drafting refers to the trapping of the trailing particle in the wake of the leading particle (also known as inertial wake suction). Kissing refers to vertically aligned particles that touch or nearly touch each other and which is a highly unstable configuration. Finally, tumbling happens when particles are reorganized from vertically aligned during kissing to horizontally aligned during tumbling.

Jayaweera et al. in 1964 [26] studied the structural instability in sedimenting suspensions and found that clusters composed of 2-6 spheres fall faster than a single sphere at Reynolds numbers in the Stokesian regime up to 10, but when the number of particles increases above 6, the clusters split and form stable sub-groups of clusters as can be noticed on the left in Figure 1.9.

Focusing on the structural instability in fluidizing suspensions, Kajishima et al. [27] was the first to notice the formation of columnar structures after passing a certain Galileo number. Furthermore, Uhlmann and Doychev [28] numerically found similar results that after passing a critical Galileo number, the particles form a columnar structure as shown in Figure 1.4. The results were experimentally validated by Huisman et al. [29], however, both of these studies were performed on a sedimenting suspension under different ranges of Galileo number ($110 \leq Ga \leq 310$). The results showed that at a very dilute regime, enhance settling is observed due to the formation of clusters. When Φ increases, the columnar structure destabilizes and the fluidized particles start behaving in a quasi-random motion. In a recent study by Shajahan et al. [30], the particles are preferentially settling in horizontal particle pairs in the intermediate concentration regime (2% ≤Φ ≤10%).

Several studies have focused on investigating the drag force acting on spherical particles and how drag reduction can influence the formation of particle clusters. These studies have compared flow regimes at different solid volume fractions and Reynolds numbers. The flow regimes are usually categorized depending on the author. Liu et al. divided the regimes into either dilute ($\Phi = 0.1\% - 3\%$) or loose ($\Phi = 3\% - 40\%$) [31]. Even in the dilute regime, the wake structure of individual particles is affected, as observed in Figure 1.5. The figure illustrates the difference in the wake structure between a single isolated particle and a particle surrounded by eight other spherical particles. The wake length is significantly reduced, and the axisymmetry is disrupted [32].

Moreover, the solid volume fraction Φ has a significant impact on the flow regime. At Φ values below 3%, the particles aggregate vertically in a relatively stable manner. For Φ values between 3% and 10%, there is no vertical aggregation, and the kissing mechanism between particles is highly un-

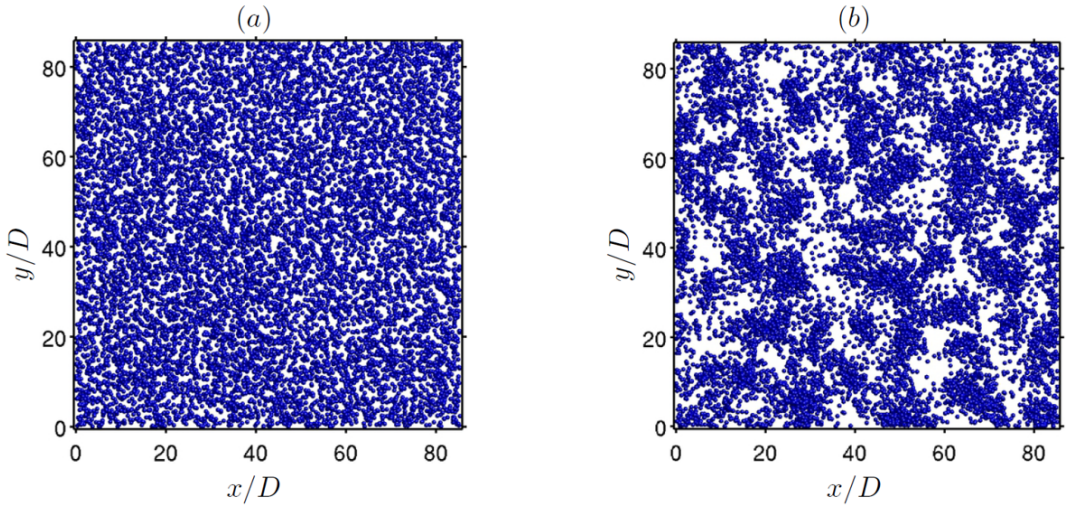

Figure 1.4: Particle positions viewed from the top view of columnar structures seen in DNS at (a) Ga = 121 and (b), Ga = 178. [28].

stable. In this moderately dense regime, there are relatively stable horizontal doublets, and there may be interference of DKT-type instability with the passage of kinematic waves. For Φ values above 10%, the regime is considered to be loose or dense, with a hard-sphere distribution and smoothly varying velocity spectra [19]. However, it is still unclear how these flow regimes differ for various Galileo numbers under different inertial effect.

At the loose regime, dense clusters of particles are formed, which behave differently from the dilute clusters that are formed. In the presence of dense clusters, the cluster effects are dominant in the direction perpendicular to the flow, leading to high shear stress, also known as hindered settling, which results in an increase in the drag force on the particles. Conversely, drag reduction is observed in the dilute clusters, where the cluster effects are dominant in the flow direction, leading to a suction effect of the rear particles, also known as drafting-kissing.

The clusters are divided into long-lived and short-lived clusters, with numerical studies showing that at low Archimedes number ($\sqrt{Ar} = Ga$), the clusters formed belong to the long-lived category, resulting in hindered settling, while at relatively higher Archimedes numbers, short-lived clusters are formed, resulting in reduced hindered settling [33]. It is worth noting that Archimedes number and Galileo number are used interchangeably in the literature.

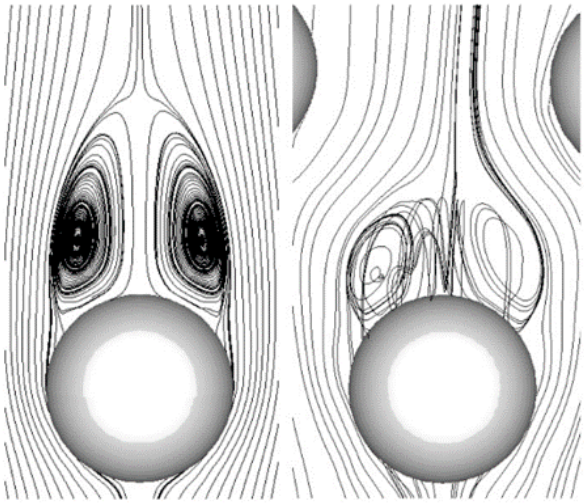

Figure 1.5: Wake of a single sphere settling in infinite medium vs sphere settling in the presence of eight other surrounding particles at $Re_\infty = 200$ [32].

1.2.3. Inverse fluidization

Inverse fluidization as a hydrodynamic phenomenon is the study of light-rising spheres in a fluidized suspension where the fluid is flowing against the particle's motion as can be seen in Figure 1.6. Interesting results were discovered in the inverse fluidization experiments, especially relevant to the bioreactors [34], anaerobic biological processes due to their high mass transfer potential [35], and wastewater treatment [36].

Early experiments on inverse fluidization were first conducted in 1982 by Fan et al. [38], where spherical floating particles were inversely fluidized and the hydrodynamic characteristics of the phenomena were studied. Inverse fluidization was further studied by Nikolov et al. [39]. The study was more related to the uncontrolled growth of the fixed biomass in biofilm reactors and how it affects the hydrodynamic characteristics of each bioparticle. Further experiments were performed by the same group [1] as the concept of using inverse fluidization in the bioreactor engineering industry was very promising as the biofilm thickness can be controlled.

In these extensive experiments, particle densities were varied between 75 - 930 kg/m^3, with tap water as the working liquid, and experiments were done in the Galileo number range of 161 - 1260. The results obtained are in agreement with Richardson and Zaki's famous correlation between fluidization and sedimentation. Different experimental studies were done throughout the years on the hydrodynamics [37], bed expansion, pressure drop [36], minimum fluidization velocity [40], and voidage characteristics in an inverse fluidized bed [35].

Prediction and calculation of the minimum fluidization velocity as well as the pressure drop in the fluidized bed is a very important parameter for the efficient and economical operation of the reactor as it is closely related to the efficiency and energy demand in these processes. It was found that similar correlations can be applied in inverse fluidization given that the mass density of the particles does not go below 300 $[kg/m^3]$ [1]. The fluid flow rate is an important factor in fluidization and sedimentation, as it determines the forces acting on the particles and the overall performance of the system. However, there is still a lack of understanding of how the fluid flow rate affects the fluidization and sedimentation of particles, and how it can be controlled to optimize these processes.

In fluidization experiments, there is a range of fluid velocities at which the experiments should be conducted. The fluid velocity needs to be above the minimum fluidization velocity, to ensure a homogeneous suspension is present and that the packed bed is fully fluidized. The maximum fluidization velocity needs to be avoided to avoid any unstable scenario. Minimum fluidization velocity is also referred to as the on-set of fluidization. With further increase in flow rate, more and more particles get

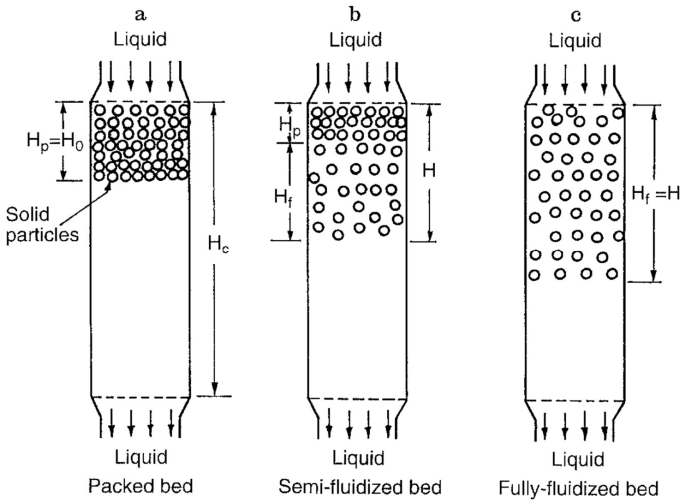

Figure 1.6: Schematic representation of steps encountered in two-phase inverse fluidization process [37].

detached from the packed bed. Bed height increases linearly as the downward force due to the liquid overcomes the upward buoyancy forces due to the low-density particles reaching a level where the pressure gradient within the bed is minimum [36].

The maximum fluidization velocity is calculated to be on the same order as the terminal velocity of a single settling sphere. Once the minimum fluidization velocity limit is reached, and with a further increase in liquid velocity, the voidage between the spheres increases. This may cause a gentle slugging and bubbling motion in the bed. For a liquid velocity corresponding to a bulk solid volume fraction of 0.3, the particles exhibit the most active local motion. At this Φ, a root mean square (RMS) value reaches its maximum value. Macroscale effects such as solids circulation, and wall-to-fluid heat, and mass transfer start dominating as the thermal Peclet number is at maximum in this bulk solid volume fraction [35]. Peclet number is the measure of the rate of advection to the rate of diffusion ($Pe = Lu/\alpha$). L is the characteristic length, u the local flow velocity, and α is the thermal diffusivity. As Pe increases, Brownian effects become less predominant and the viscosity decreases.

Solid circulation occurring in fluidization and sedimentation, also known as intrinsic convection, usually occurs due to the depletion of particles near the wall [41]. The confinement caused by vertical walls would provide a cut-off for the velocity field fluctuations and further induces an intrinsic convection of the suspension [42]. Figure 1.7 shows intrinsic convection taking place in a confined geometry for a sedimentation experiment. The same phenomenon of intrinsic convection is witnessed in fluidization experiments during this thesis.

Bruneau et al. [43] mentioned that the main reason behind intrinsic convection is that the weight of the suspension is smaller near the walls, driving the convective motion. In their numerical study, a model was developed that predicts the intrinsic convection is reduced nearly to zero at a volume fraction $\Phi = 0.2$. It is also predicted that the intrinsic convection decreases with increasing particle volume fraction.

Peysson et al. [44] did another experimental study on the magnitude of intrinsic convection in sedi-

menting suspension. They found that at lower concentrations, there is a small magnitude of convection and that vanishes at large concentrations. This is caused because of an ordering of the suspension near the wall that induces intrinsic convection. The amplitude of the intrinsic convection is found as a function of particle volume fraction. Surprisingly, no convection is measured at a low volume fraction ($\Phi = 5\%$). However, as the volume fraction increases ($\Phi = 10\%$), the particles settle faster in the center of the cell than near the side walls. Further increasing the volume fraction ($\Phi = 20\%$) causes the amplitude of the convection to diminish. They have also claimed that there may even be convection in the opposite direction at ($\Phi = 30\%$). However, this was not proved as if the magnitude was very small, it would have been within the limit of their experimental resolution.

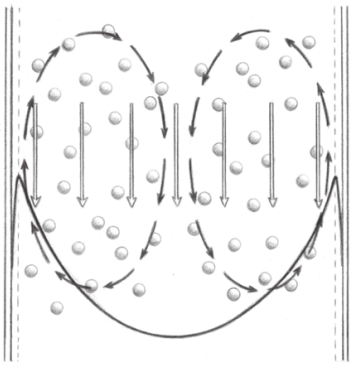

Figure 1.7: Schematic of intrinsic convection in a sedimenting suspension [41].

1.2.4. Liquid-Solid fluidization in a rectangular channel

One of the first studies on 2-D fluidization was performed by Volpicelli in 1966 [45]. It showed that the Richardson and Zaki correlation developed for 3-D fluidization can be applied to 2-D fluidization with an offset factor. 2-D fluidization experiments are usually performed in a narrow channel with a distance between the plates in the same order as the particle diameter. Having this narrow distance between the plates restricts the movement of particles in the 3rd dimension. This facilitates direct optical access for particle tracking. Experimental investigations for dilute suspensions for observing cluster formation were done by Jayaweera et al. [26], which later lead to the famous results obtained by Fortes et al. [25] in a 2-D fluidized bed at various Reynolds number up to 1800.

Furthermore, different researchers studied the wall effects on a terminal velocity for a single sphere. Some studies focused on circular and non-circular ducts [18, 46], while other studies were regarding the settling of non-spherical particles [47]. In a recent review paper by Yao et al. [48], different factors affecting the settling velocity of a particle were studied. These include the wall retardation effects in different confined geometries.

Different correlations were developed for predicting the confined terminal velocity, whether depending on Re, or the shape of the geometry [49]. To account for the wall effects, which can be highly significant for laboratory-scale experiments, particularly in 2-D fluidization, Garslde et al. [50] developed another correlation that relates the particle's terminal velocity to with the wall effects, before using R-Z correlation. Yao et al. [48] concluded that the correlations developed do not produce the same curves, suggesting that the effect of wall retardation on particle settling depends on many other factors in addition to the size ratio. The factors include fluid rheology, particle structure, and particle surface characteristics.

Other researchers developed various models for predicting the terminal velocity of a single settling sphere under different conditions. Zhu et al. [51] compared the geometric similarity of cylinder, annulus, and parallel plates to develop a relationship between three wall effects. A unified model is reached that predicts the settling velocity at a relatively high accuracy (10%), and is suitable for different geometries. To study 2-D liquid-solid fluidization rather, the following two features must be considered. Firstly, the

study about inertia that leads to the formation of wakes behind the particles thus affects the anisotropy of the microstructure. Secondly, the difference between 2-D and 3-D fluidization experiments is the much more pronounced effect of lubrication forces exerted from the walls on the fluid and the particles in the 2-D case [1, 52].

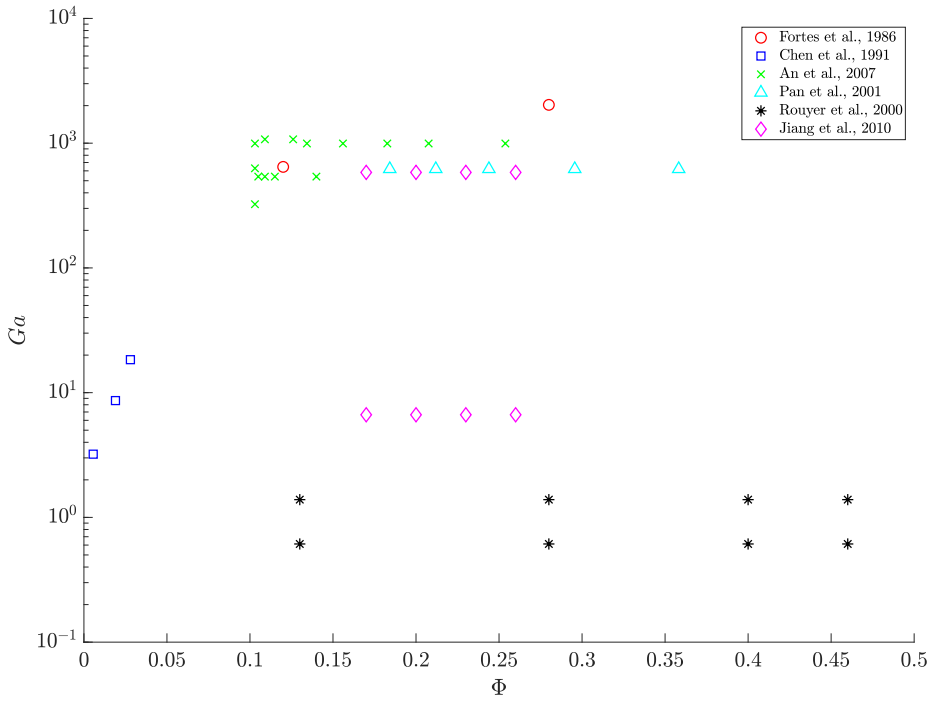

Figure 1.8: Regime map summarizing all fluidization experiments performed in a rectangular channel in terms of Ga vs Φ.

Different experiments were performed on 2-D liquid-solid fluidization are summarized in Figure 1.8. Figure 1.8 is a regime map with an overview showing all the prominent experiments done in this field, and clearly identifying a gap between Galileo number in the range of 20-500. For the regime map, when Ga was not provided in the reference, it was estimated by using Abraham's empirical correlation [53] for the drag coefficient based on Reynolds number (see section 1.1).

Fortes et al. [25] was the first to observe the local mechanisms involved in fluidization that include DKT into stable cross-stream arrays. The experiments were performed in 2-D and 3-D fluidization, where several particles were tracked. DKT mechanisms can lead to the formation of clusters or aggregates of closely packed spheres. These can align in contact along vertical lines through their centers. The transition from kissing to tumbling in fluidized beds can be influenced by factors such as the fluid flow rate, particle size and shape, and particle concentration in the bed. This transition can have an impact on the fluidization and mixing performance of the bed. These different flow regimes that were observed in the experiments are dominated by the inertial effects associated with wakes. These effects are important even at low Reynolds number, where the drag on the particles is thought to be due to the wake suction of the leading particles. Smaller particles and irregularly shaped particles are more likely to form clusters and exhibit kissing behavior, while larger and more spherical particles tend to tumble and rotate more easily as this is a highly unstable scenario [54]. The particle concentration in the bed is found to affect the transition from kissing to tumbling, with low concentrations leading to more kissing and high concentrations leading to more tumbling.

Fortes et al. [25] found that the mechanisms of DKT are present in an inclined fluidized bed, in a 2-D fluidization column, as well as a 3-D fluidization chamber as can be noticed in Figure 1.9. In

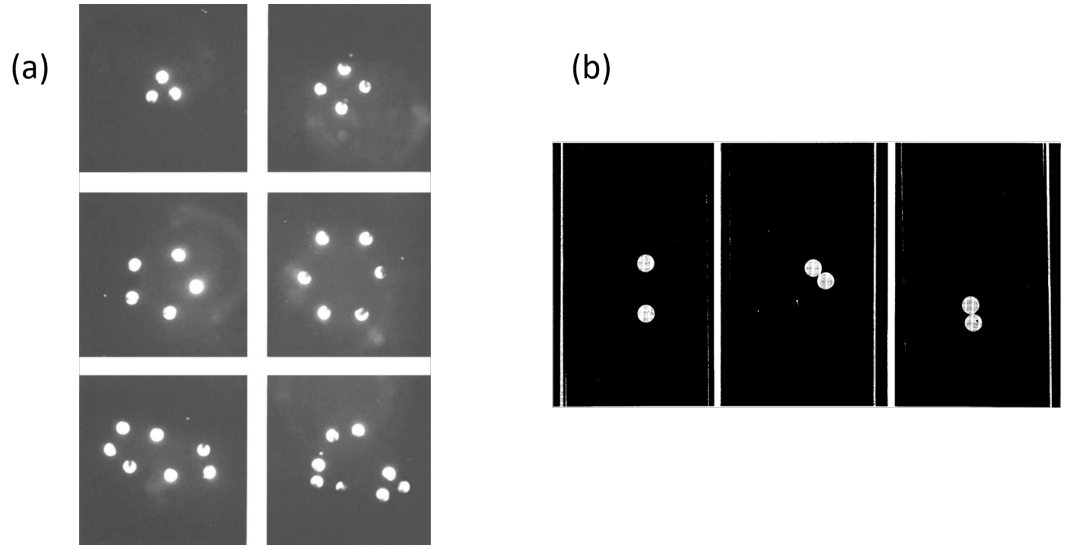

Figure 1.9: (a) Cluster formation and disintegration in a fluidized suspension. Maximum of 6 particles are formed in a cluster, then disintegrate to smaller clusters [26]. Visualization of DKT-type instability in the sedimentation experiments by Fortes et al. [25].

Fortes et al. experiments, the Reynolds number was set at 650 for a vertical channel but was slightly higher ($Re = 730$) when the channel was inclined at 23°. Since the walls have dissipative effects that increase the stabilizing effects of wall friction at that inclination. The results demonstrate that DKT-type instability is present in fluidization/sedimentation studies regardless of inclination or wall effects.

Different studies were conducted on 2-D fluidization motivated by the study from Fortes et al. [25]. Chen et al. [54] studied the formation and disintegration of particle clusters. The microstructure analysis shows that when a cluster forms, particles organize themselves in a vertical direction, whereas the disintegration of a cluster leads to a horizontal alignment of the particles, which gradually disperse into individual particles or small clusters. The results indicate that the degree of particle clustering initially increases, reaches a maximum at Re = 3, and then decreases with an increase in the Reynolds number within the range of 0.662 to 10.88 at a fixed solids concentration of 0.019. Chen et al. [54] claimed that the clustering phenomenon is most pronounced within an optimum range of Reynolds number in Oseen's regime. The authors recommend further investigations into the continuous formation and disintegration of clusters in sedimentation and fluidization systems within the Reynolds number range studied, using advanced visualization techniques such as high-speed imaging and particle tracking methods.

Another study by Rouyer et al. [55] focused on the viscous-dominated regime. The 2-D fluidization experiments, the suspension showed localized channelized structures, similar to those observed in low-porosity media. Cluster formation and disintegration were observed, resulting in non-Gaussian probability density functions (PDFs) attributed to particle-particle interactions. Vertical clusters were formed by particles moving downwards at low velocities. Inertia was not significant in these macroscopic particle experiments. The authors claim that particle-particle interactions play a dominant role in cluster formation and dynamics in viscous-dominated flow suspensions.

Pan et al. [56] performed a numerical and experimental fluidization study for 1204 particles in an inertial-dominated regime. The authors compared their experimental findings with DNS (direct numerical simulations) results for verification. An et al. [57], performed a wide set of experiments at different bulk solid volume fraction to study the clustering formation in an inertial regime as well. The authors used a CCD image measuring and processing technique to analyze the clustering behavior of solid particles in a liquid-solid fluidized bed, as well as the use of fractal analysis to characterize the microstructures found in the fluidized bed. The fractal analysis is a mathematical method for describing complex geometrical structures, and the cluster configurations are often in the form of horizontal strands.

Finally, Jiang et al. [58] conducted experimental work to investigate the microstructure of the solid phase in fluidized beds for non-Stokes regimes. The study included experiments at Galileo number (Ga) at two different orders of magnitudes, O(10) and O(500). The main findings of the study were that the microstructure of the solid phase was anisotropic due to the formation of wakes behind the particles caused by inertial effects. The pair probability distribution function and structure factor were used to characterize the microstructures, with the pair probability distribution function presenting a similar shape for all ranges of parameters. Additionally, when inertial effects became significant (Re > 100), the solid phase became stratified by the formation of horizontal chains. However, the origin of this stratification remains uncertain.

1.3. Goals and research questions

Few literature studies have been conducted on 2-D liquid-solid fluidization as was clearly shown in the previous section, making it an appealing field of research to further study. Few experiments have been done in a viscous dominated regime [54, 55, 58], and in an inertial dominated regime [25, 56, 57]. There is a clear gap that can be explored for Galileo numbers between $1 - 400$ at all the possible bulk solid volume fraction ($0.05\% - 45\%$).

Currently, there is limited knowledge regarding the potential changes in microstructure and associated flow dynamics when increasing the Ga and varying Φ. How might the changes impact the transition in a viscous or inertial-dominated regime. This study focuses on the structure and dynamics of a fluidized suspension by investigating the competing effects of wake trapping, drafting-kissing-tumbling, and multiparticle interactions. This thesis focuses on exploring the influence of inertia by varying Ga over a wide range of concentrations. Experiments were done at 3 different Ga numbers 147, 196, and 252.

The goal of this research is to analyze the macroscopic properties of fluidized suspensions, to study the clustering of particles in dilute suspensions, and to bridge the microstructure of the suspension with the macroscopic properties. The main two research questions are given as follows:

1. What is the role of inertia in inverse fluidization?
2. To what extent is the anisotropy of particle distribution affected by inertial hydrodynamic interactions between particles?

To address these questions, the approach used in this study is to experimentally investigate a 2-D inversely fluidized bed in an optically transparent narrow rectangular channel. The Galileo number will be varied by altering the working liquid's temperature while holding the particle diameter and density ratio constant. The microstructure of the suspension will be characterized using PTV measurement techniques. The effects of inertial hydrodynamic interactions on particle distribution and clustering will be studied. By answering these questions, a better understanding of the phenomena of fluidization at different Galileo numbers and bulk solid volume fractions can be gained, filling a gap in the current literature. During this approach, possible errors and uncertainties in the results will be considered to ensure their reliability.

2

Experimental Methodology

This chapter covers the experimental methodology, followed by the respective measurement systems and techniques. Initially, the experimental setup is shown, including its constraints and design philosophy. The primary fluidization column and all the sensors used in this experimental setup are shown. In Section 2.1.1, the spherical particles used in the experiments and the working liquid to estimate the Galileo number are shown. Section 2.2 focuses on the LabVIEW program developed for data logging, while Section 2.3 explains the optical measurement methodologies. Section 2.4 addresses the experimental procedure. Section 2.5 presents the post-processing operations. Section 2.6 provides a brief summary of the overall experimental methodology, starting from the experimental setup to the fundamentals of the PTV code, to calculating the velocities profiles.

2.1. Experimental Setup

A schematic representation of the experimental setup is shown in Figure 2.1, and the final version of the built-up experimental setup is shown in Figure 2.2.

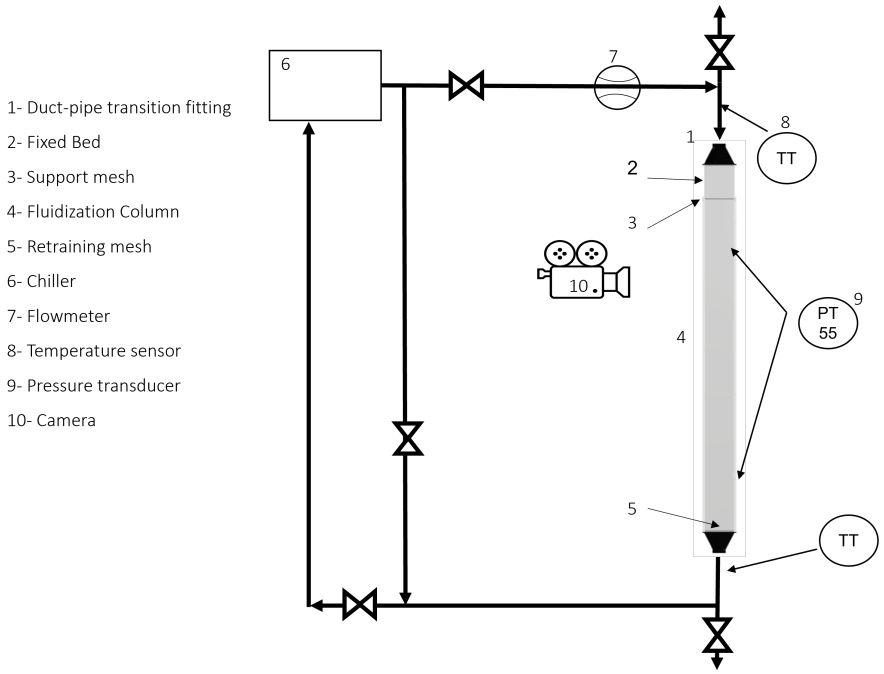

Figure 2.1: Schematic representation of the experimental setup. The different components are labelled on the figure.

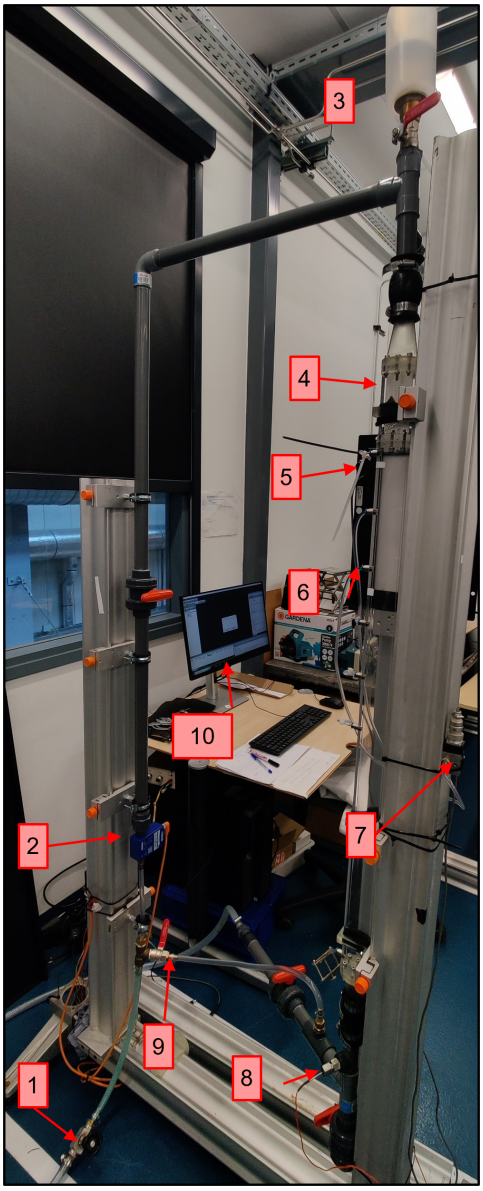

Figure 2.2: Constructed experimental setup with the different components. 1. Needle flow-valve, 2. Flowmeter, 3. The degassing system, 4. Fixed bed, 5. Light source, 6. Fluidization column, 7. Pressure transducer, 8. Temperature sensor, 9. Bypass valve, and 10. Workstation.

Taking a close look at the schematic (Figure 2.1), at the entrance of the fluidization column, a 3D-printed transition fitting (1) is installed to ensure a smooth flow transition from the circular pipe to the rectangular duct. The liquid goes through a packed bed (2), acting as a liquid distributor. The liquid distributor, placed at the entrance of the column, is built in a way to ensure homogeneous liquid distribution across the column's cross-section. A support mesh (3) is positioned at the base of the packed bed, immediately above the main fluidization column (4), to prevent particles from leaving as shown in Figure 2.3.

The fluidization column is constructed using transparent PMMA (Polymethyl methacrylate) to facilitate direct optical access. It comprises two parallel PMMA plates, each measuring y = 1000 mm in length and x = 54 mm in outer width (inner width = 45 mm), with a thickness of 10 mm to ensure rigidity. This rigidity is essential in maintaining a constant gap of 3.5 mm between the plates. The PMMA plates were precisely milled and adhered to ensure high manufacturing tolerances ($\pm 0.127mm$). The thickness of each plate (1 cm) is large enough to avoid bending.

The fluidization chamber is equipped with seven pressure taps to monitor pressure drop. The first six are uniformly distributed at intervals of 10 cm, and the final tap is situated just at the end of the column ($y = 975mm$). This arrangement aims to ascertain a consistent pressure drop during the full fluidization of the suspension. Additionally, one must consider the potential for algae growth in the chamber and on the particles when handling multiphase flow. Therefore, a detachable design for the experimental setup has been adopted to facilitate easy cleaning. Detailed technical drawings of these components can be found in Appendix A. Another retaining mesh (5) is placed to avoid particles from leaving from the fluidization column to the pump.

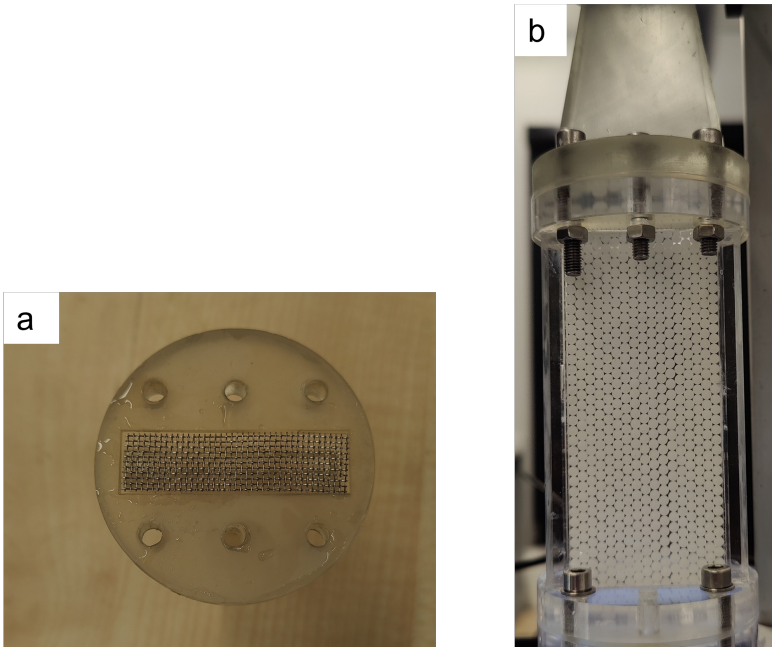

Figure 2.3: Detailed pictures of an (a) 3D printed transition fitting with mesh, and (b) Fixed bed designed for liquid distribution.

The flow is in a closed-loop configuration through a centrifugal pump integrated within the chiller (6), which is stationed at the highest elevation point within the setup. The reason behind placing the chiller at the highest point is to create a slight overpressure in the system. This will prevent gas from entering the experimental setup, in case one of the valves was not perfectly sealed. The chiller is a Lauda RP 845 (see Figure 2.4a), and is used to regulate the temperature. It operates within a temperature range of -30 to 300°C, enabling precise temperature control (0.01°C) for the experiments. The built-in centrifugal pump possesses a pressure suction of 24/18 (L/min), and the thermostat accommodates a maximum filling volume of 7.5 liters. A low-flow needle valve (see Figure 2.4d) is placed to precisely control the volumetric flow rate.

Flow rate is measured using a MAG-VIEW Low-flow Magnetic Inductive Flow Meter (7) (series: MVM-002-Q), see Figure 2.4e. The flow meter has the capacity to measure a flow rate range of 0.1-2 (L/min) with an accuracy of ±1% RD (percentage of reading). It generates a pulse output at a rate of 1000 pulses per liter and is interfaced with a USB-6009 DAQ card for recording pulse output via a LabVIEW program.

PT100 temperature sensors (8) are installed at the inlet and outlet of the fluidization column to ensure temperature uniformity throughout the experiments. Additionally, a Validyne DP15 differential pressure transducer (9) is employed, featuring an accuracy of ±0.5% of the full scale. The full scale is contingent on the diaphragm utilized; in this instance, diaphragm 28 was used, exhibiting a full scale of 5.5 kPa, translating to an uncertainty in pressure measurement of ±27.5 Pa. The pressure transducer was calibrated for a maximum pressure differential of 7 kPa, and the calibration curve is added in Ap-

pendix B.

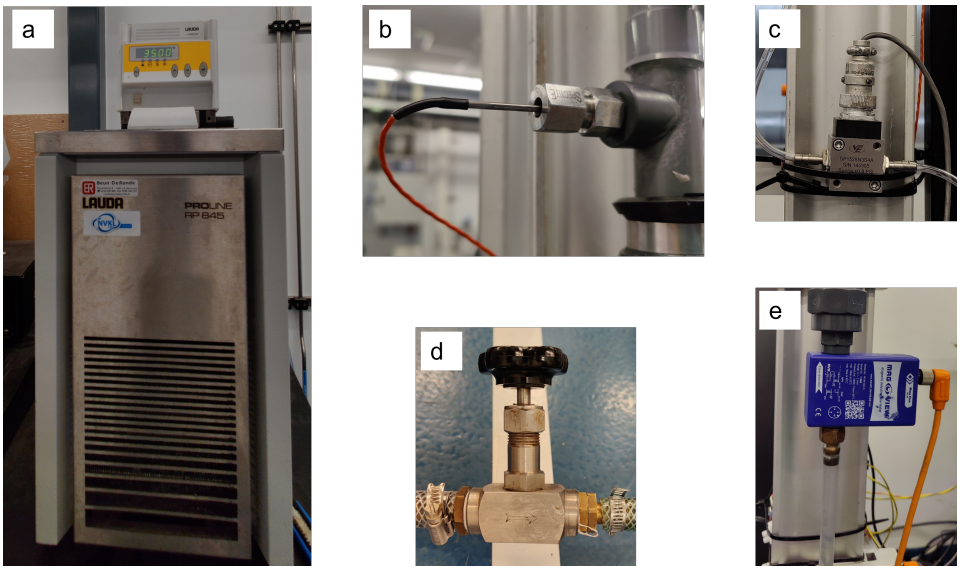

Figure 2.4: Sensors used in the experimental setup including a. RP 845 chiller, b. PT100 temperature sensor, c. Validyne DP15 pressure transducer, d. Needle flow-valve, and e. MAGVIEW magnetic flowmeter.

2.1.1. Estimation of Galileo Number

Accurate estimation of Ga was crucial to the experiments. Ga is heavily influenced by the diameter and density of the particles, as well as the fluid's viscosity and density. Polypropylene (PP) precision balls (RGP balls) are used to reach the desired range for this study. These PP balls are characterized by a diameter of 3 mm, a density of 870 kg/m^3, water absorption of 0.01% Aw (water activity) for 24 hours, and a coefficient of thermal expansion (α) of $135.0 \cdot 10^{-6}\ °C^{-1}$. The precision balls purchased from the supplier were of grade I. The supplier provided a maximum diameter tolerance of $\pm 25[\mu m]$ and a sphericity tolerance of $\pm 12[\mu m]$. Manufactured through injection molding, the balls underwent lapping finishing to achieve high tolerances.

The experiments were done Ga of 147-255. Consequently, only water was used as the working liquid. Following careful measurements of particle diameter and density, the particles used in the experiments had a density range of 870 < ρ_p < 876 [kg/m^3] and a diameter of 3.002 mm. Details of these measurements are shown in Appendix C. The following section presents the spherical particles selected as well as the thermophysical properties of the working liquid to achieve the desired Ga.

Based on the chosen working fluid, spherical particles, and restrictions on maximum dimensions, the experimental setup was carefully designed. The representation of this setup is shown in Figure 2.2. The parameters employed within the system led to a liquid-solid density ratio of 0.87. Throughout these experiments, the Galileo number was maintained within a range that ensured a steady wake formation with planar symmetry. These experiments are intrinsically dependent on the Galileo number (Ga), volume fraction (Φ), and the ratio of particle diameter to the characteristic length (D_p/L).

The quality of the spheres was a critical factor in the experimental procedure, particularly in estimating Ga. The diameter was measured using a camera, capturing 130 images with each image containing around 25-30 spheres as can be seen in Figure 2.5. The diameter was calculated employing a Circular Hough transform method in Matlab, resulting in a standard deviation of 0.013 mm, and a percentage error of less than 0.5%.

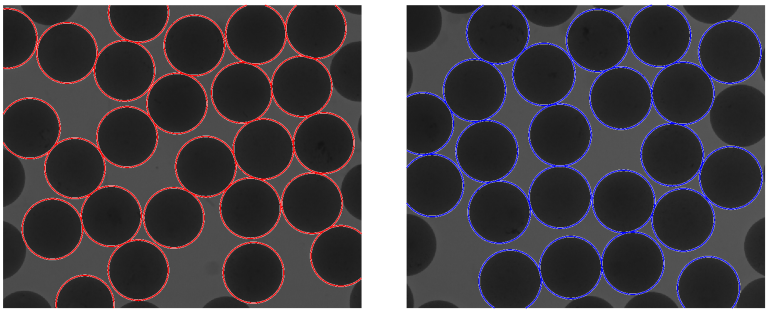

Figure 2.5: Images exported from MATLAB showing spheres detected.

To measure the density of the spheres, a sink-float density match method was employed. Around 600 gr of the particles were placed in a cylindrical beaker filled with acetone. The collective mass was measured to establish a ballpark of the average density. Subsequently, acetone and tap water mixtures were prepared to achieve densities of 870 and 885 [kg/m^3], respectively. The spheres were agitated to ensure wettability, allowed to settle, and outliers were removed. Followed by that to calculate the density, the mass of the spheres had to be found first. Initially, 30 petri dishes were used, with each dish holding 12 particles. The average mass of a single particle was computed by dividing the total mass by 12. Due to the manufacturing process of the PP spheres, vacuum voids may occur in the spheres, causing a density lower than the measured and averaged density. The standard deviation is taken for all these measurements. The data were analyzed with a confidence level of 95%, which corresponds to a t-value of 1.699. In appendix C, the detailed approach to the measurement procedures is provided. This includes the steps involved in evaluating the mass and diameter of the particles, which were critical in determining their density.

2.2. Data Acquisition System

A National Instruments USB-6009 DAQ (Data Acquisition) card was integrated into the experimental setup and interfaced with a LabView program. The DAQ card was configured with four inputs; one counter for recording pulses from the flowmeter and three analog inputs. The differential pressure transducer operated on voltage output, while the PT100 sensors utilized a 4-20 mA output. For the PT100 sensors, a high-precision 500 Ω resistor was employed to convert the 4-20 mA output to 2-10 V.

Temperature readings initially exhibited considerable noise, thus the integration of a 2nd order low-pass Butterworth filter to enhance reliability was necessary. The filter had a high cutoff frequency of 0.45 Hz and a low cutoff frequency of 0.125 Hz, with a sampling frequency of 1 Hz. Accurate temperature measurements are critical as they influence the Galileo number. Maintaining a consistent temperature at the top and bottom of the fluidization column ensures steady values for the working liquid's density and viscosity.

Pressure data was acquired through a calibrated pressure transducer, and the calibration curve was integrated into the LabView code. Integrating the calibration curves into the LabView program saves time while extracting the data. Waveform graphs were plotted for temperature and pressure readings, where fluctuations could be observed. Calibration curves were fitted for both temperature and pressure sensors. To obtain the calibration curve for the pressure transducer, the pressure was altered using known values, and the corresponding voltage output was recorded. The temperature sensor calibration curve was already given by the supplier.

The flowmeter readings were recorded, and the k-factor was adjusted according to the pulses per liter for the flowmeter. This flowmeter generated 10,000 pulses per liter. The flowmeter was calibrated as well to ensure accurate recordings are obtained. In an empty beaker, the time was recorded to fill

up 1 liter, and compared with the results obtained from the flowmeter. In the LabView program, the flow rate was displayed in liters per minute. After completing each experiment, the data was automatically exported for plotting and further analysis. The data was filtered by excluding the initial 1-minute readings until the flowmeter began recording stable data.

2.3. Camera Calibration

A calibration of the fluidization column is essential to obtain an accurate conversion factor from the camera's coordinates (px) to real physical coordinates (mm). This conversion factor (unit: px/mm) is required for accurate particles displacement, especially near the edges where the picture might be affected by distortion. The calibration grid consists of a rectangular pattern of circles (see Figure 2.6), which are 5 mm apart. The panel has a depth of 3 mm, and width of 44 mm. It can just fit in between the rectangular fluidization channel. The initial calibration grid for the setup had a total length of 10 cm (see Figure 2.6). The conversion factor of the camera was 23 px/mm. Although this configuration provided exceptionally clear images and videos, it was not possible to track enough particles over time. In a fluidized suspension, particles near the edges leave and join the field of view (FOV). Consequently, a longer calibration grid was used, which had a similar pattern but allowed for a FOV of 21 cm. The camera was positioned at an appropriate distance from the setup based on the calibration grid.

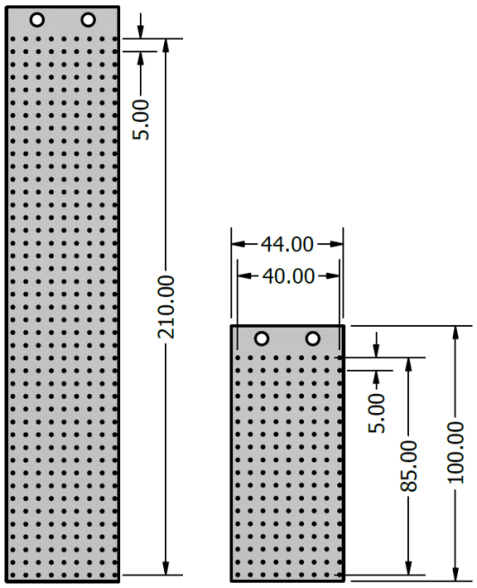

Figure 2.6: Technical drawing of the calibration grids obtained for the experimental setup.

Initially, it was thought to obtain a transform function to precisely map the image. However, if the influence of distortion is negligible, and within the camera's resolution, then a first-order transform function (conversion factor) is sufficient. To accurately obtain this conversion factor, the following method was followed. The circles on the calibration grid were all detected on MATLAB using imfindcircles, then straight horizontal and vertical lines were fitted passing through the circles. Finally, the distance between each of these distances is obtained in pixels. For the horizontal and vertical scaling, the real distance between each of these circles is 5 (mm). The mean average between each of these circles was given to be 48.54 ± 0.51 px (95 % confidence interval). This gives a conversion factor of 9.7085 ± 0.102 px per mm in all directions. It follows that the leading uncertainty is the uncertainty of the camera. This is because from the calibration an uncertainty of 0.51 px is found, which is smaller than the resolution (1 pixel) of the camera. Despite employing a calibration grid for pixel-to-millimeter conversion, potential sources of error in diameter measurement remained. These include camera magnification, calibration grid, and lighting.

A LaVision imager pro-sCMOS camera is used in the experiments. The diaphram aperture $f_{\#} = 16$

is used with a range of images of 2016x2016 pixels. When extracting the image sequence, to save up memory, only the FOV (2016x430 pixels) was extracted. The camera's frame rate was chosen, adhering to the Nyquist sampling theorem, to be more than twice the frequency determined by the gravitational timescale of the spheres

$$t_g = \sqrt{D_p / \mid \overline{\rho} - 1 \mid g}, \tag{2.1}$$

ranging from 100 to 200 Hz depending on the case under investigation. A rear LED panel ensured adequate illumination and contrast between the particles and the bed. The particles within the moving suspension appeared as dark circles against a brightly illuminated background. Figure 2.2 illustrates how the LED panel was fixed behind the column. The camera was connected via an Ethernet cable for data transfer, and the pro.camware software was used for recording and extracting image sequences. Post-experiments, Particle tracking velocimetry (PTV) code was employed, and the videos were processed using MATLAB.

2.4. Experimental Procedure

For accurate and repeatable fluidization experiments, a comprehensive procedure was always followed. The procedure began with wetting the spheres in water for at least 30 minutes. To ensure the complete detachment of air bubbles that could influence the results. The PP spheres were then mixed with Polyethylene Glycol (PEG) surfactant at the minimal critical micelle level. To reduce the possibility of air bubbles attaching to the surface and to avoid soap bubble formation. Subsequently, the spheres were added to the fluidization column. Ensuring consistency in the formation of the bed was critical for maintaining homogeneous inflow conditions across all experiments. Thus, a different set of spheres were carefully inserted into the packed bed.

Once the system was closed, it was gradually filled. A bypass from the chiller was employed to enable simultaneous filling from both sides at a slow flow rate. This was necessary to fill up the system and reduce the formation of air bubbles on the column. The degassing valve was left slightly open. This ensured the removal of any air bubbles that could affect the hydrodynamic interactions between the spheres.

After the complete removal of air, the system was kept running for 30 minutes with a flow rate of 1.5 L/min. The desired temperature was set using the chiller and was verified using PT100 temperature sensors at the column's inlet and outlet. As the temperature reached the desired level, the column was gently fluidized until the desired bulk solid volume concentration was achieved. For an initial guess for the concentration, a measurement tape was placed alongside the fluidization column, and an estimate of the concentration was obtained. This was further validated after performing the experiments by counting the number of particles in the field of view. The downward fluid velocity controls the bed expansion, as well as the concentration. At low flow rates, the bed is close-packed, until the fluidization velocity surpasses the minimum fluidization velocity resulting in a homogeneous suspension. To ensure the system achieved a steady state, the fluid velocity was held constant for about 10 minutes after reaching the desired concentration. This provides a reliable basis for interpreting the experimental outcomes.

Data recording is done using the LabView program mentioned and by video capturing with the camera at 165 frames per second (fps). After recording, the LabView program was turned off, and the image sequences were exported for PTV analysis.

2.5. Post processing

After recording the desired movies with the aforementioned fps, the images are processed. For a detailed analysis, a PTV algorithm is developed on MATLAB. All the scripts written for analyzing these experiments are added to a google drive link [1].

It is important to note that PTV requires good image quality and accurate calibration for reliable results. Factors such as lighting, focus, and camera stability are crucial for obtaining high-quality images. It is also necessary to have a sufficient number of particles in the field of view throughout the video for statistical convergence. An appropriate recording speed to capture the particle dynamics accurately is needed as well.

The code used in post-processing is designed to import a video, detect particles, correlate them across frames, and calculate their velocities. Following is a detailed explanation of each part of the code: Initially, the code starts by calculating the number of frames in the video. The step size can be altered depending on the sampling frequency required for each case. The particles are then detected in each frame utilizing a function that detects circles using circular hough transform method in Matlab. The function is critical for identifying particles in the FOV, which is a prerequisite for tracking and calculating velocities. The center positions, radii, detectability, and frame number are stored in a matrix.

2.5.1. Particle and Frame Correlation

The following part of the script correlates the particles across consecutive frames. It extracts unique values depending on the frame numbers and creates submatrices for each unique value. This helps in categorizing the particles according to the frames they belong to.

An identifier is assigned to each particle once it is within the FOV. The ‘KDTreeSearcher‘ class in MATLAB constructs a k-d tree, which is used in conjunction with the ‘knnsearch‘ function for efficient search queries. K-dimensional trees are data structures that are used for organizing points in a k-dimensional space. A k-d tree search algorithm is employed for the efficient search of particles within the frames. The algorithm tracks the particles through frames by searching for their nearest neighbors and correlating their positions. If a particle is matched, it retains its identifier; if not, it is assigned a new identifier. This loop continues until all frames are processed. They are particularly effective in applications involving multi-dimensional search keys such as range searches and nearest neighbor searches.

In this implementation, the ‘KDTreeSearcher‘ is utilized to create k-d trees for the particle positions in two consecutive frames. For tracking the motion of particles from the old frame to the new one. Two k-d trees are constructed, one for each frame.
The ‘knnsearch‘ function is then used to perform k-Nearest Neighbors (k-NN) search. This algorithm finds the ‘k‘ points in the dataset that are closest to a query point in terms of Euclidean distance. Specifically, for each particle in the new frame, the algorithm finds the nearest particle in the old frame. Similarly, for each particle in the old frame, it finds the nearest particle in the new frame. A match is established when the nearest particle in the old frame for a given particle in the new frame also has the given particle as its nearest neighbor in the new frame.

This nearest-neighbor matching is a robust way to track particles across frames, especially when the particles are moving relatively short distances between frames. It helps in determining which particle in the new frame corresponds to which particle in the old frame. Figure 2.7 shows how the PTV code initially works. Figure 2.7a shows the particles in the first frame, with black solid lines indicating where the particles are in the current frame. Figure 2.7b shows the particles in the current frame. The red outline corresponds to the predicted movement of each particle. The filled blue circles correspond to the instant position of the particle. As noticed, the displacement of each particle between two consecutive frames is small, therefore the overlap is present.

[1] PTV Matlab code built for this experimental setup. https://drive.google.com/drive/folders/1r0pVrFLpsm1xsfoasUQ22XZyhZbELtpJ?usp=drive_link

Finally, for visualization and analysis purposes, a histogram was generated to display the particle distribution in the lateral direction. This plot is to confirm the homogeneity of the flow coming out of the fixed bed. Before proceeding into the velocity calculation, the concentration of particles in the field of view is calculated. This is necessary to confirm the bulk solid volume fraction of the fluidized suspension for each experiment. For each time step, the number of particles in the field of view is counted and used to calculate the mean concentration. The generated figures gave an insight for the complications present in tracking particles in the fluidized suspension.

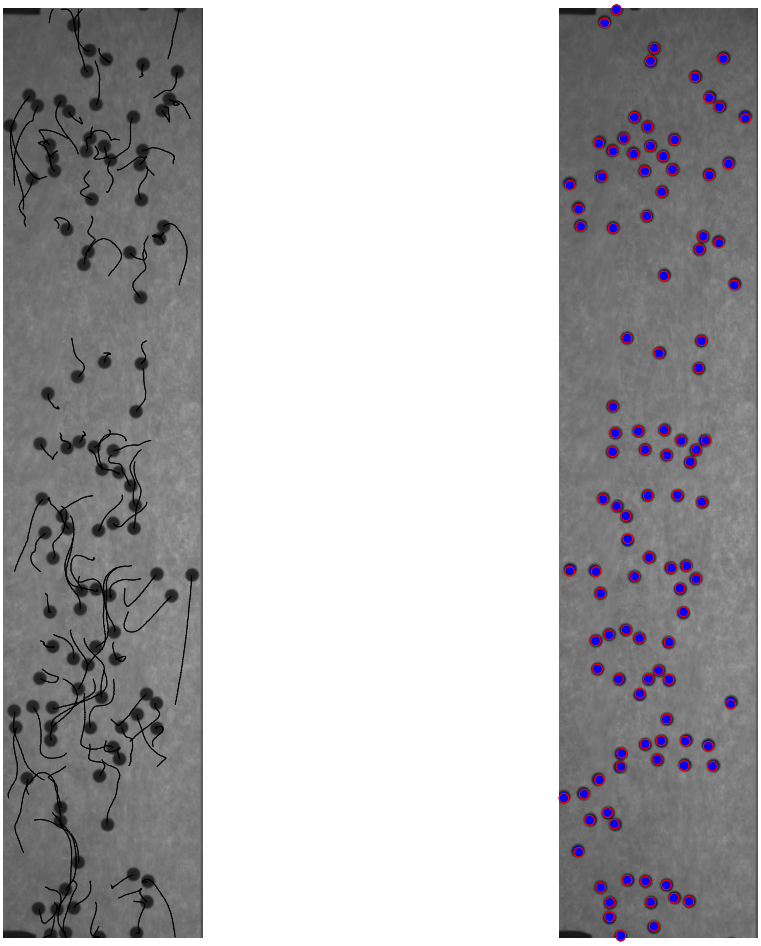

(a) (b)

Figure 2.7: Spontaneous snapshot at a certain frame showing a. The initial position of the particles with lines indicating the movement of the particles. b. A scatter plot (blue) with an outline (red) of the predicted movement of the particles in the upcoming frame.

2.5.2. Velocity Calculation

The velocity of each particle is calculated by using the differences in their positions across frames. A time step ΔT is defined according to the frame extraction rate. Pixels are converted to physical units (cm) using a conversion factor that was obtained using the calibration grid as described in section 2.3.

To translate pixel values into physical measurements, the frame rate and calibration constant from the camera settings were defined. The physical properties such as the density of the particle and fluid were specified. In the second phase of the data analysis, the position data for a specific particle was

extracted, calculated relative to its initial location, to find the trajectory. For that specific particle, the positions throughout the video frames were extracted, storing the x and y coordinates.

The unfiltered trajectory for that particle is plotted. Although the position signal was not much noisy, upon calculating the velocity, the noise is amplified. By differentiation the position, the low-frequency components are removed. Thus, the high-frequency components shows more noise on the plotted graphs. There are several ways to get rid of that noise. For the present experiments, we used the Savitzky-Golay filter. The S-G filter especially with the presence of high-frequency content along with the noise. It is important to carefully choose the filter to avoid loosing any physical meaning of the real problem. Savitzky-Golay filter consists of two main parameters, the frame length and the order of polynomial. The frame length must be odd and bigger than the order of polynomial to filter the noise. The frame length is an odd number to ensure symmetry about the center point. The polynomial order is usually much less than the window size.

To find the optimal order of polynomial for the Savitzky-Golay filter, as well as the frame length, it was an iterative process. The filter works by fitting sub-sets of adjacent data points with a low-degree polynomial by the method of linear least squares. When the data is fitted to this polynomial, the smoothed value for a particular point in the dataset is taken as the value of the fitted polynomial at that point [59]. After successfully obtaining the parameters for the filter. This polynomial can then be analytically differentiated to compute higher order statistics like velocity.

For a start, the order of polynomial for the filter was fixed at a 3rd order. The frame length was changed from 31-81 with an increment of 10. A frame length of 51 was chosen as it gave better results for that specific case. To choose the optimal order of the polynomial, the frame length was fixed at 51, and the order of the polynomial varied from 3-6. After a couple of iterations, for experiments that have a Ga of 147, and Φ of 11%, a fourth-order polynomial with a frame length of 51 was chosen. The filtered and unfiltered velocity was obtained over time. The effect of the filter on the trajectory is shown in Figure 2.8. As for the velocity, the noise becomes more prominent when the displacement is differentiated, as that is clear in Figure 2.9.

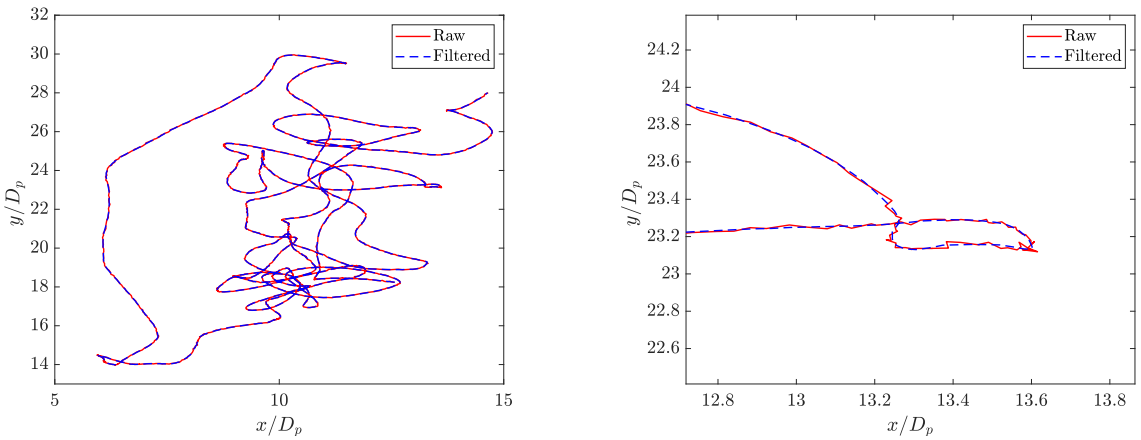

Figure 2.8: (a) Raw and filtered plots for the trajectory of a single particle in the fluidized suspension. (b) Zoomed in at sharp corners showing the effectiveness of the filter and the resulting smooth trajectory.

In conclusion, the Savitzky-Golay filter was applied to smooth the position data and estimate velocities. The window size and polynomial order for this filter were set, and the filter coefficients were calculated. The positions were filtered to remove noise, and the script calculated the velocities by taking the derivative. This was an essential step for further analysis of fluid behavior, and in the following paragraphs, it is shown how it was applied to the full suspension. An important point to note is that the filter's parameters change depending on Ga and Φ.

For the third phase during postprocessing, a more complex analysis of particle tracking data is done. This section begins by visualizing particle trajectories and then proceeds to calculate various statistics for each particle such as mean velocity profiles, velocity RMS profiles, and their pdf of the velocities normalized with the fluctuations. Finally, a concentration analysis is conducted. For the fluidized suspension, the same filter was applied to all the particles, and the trajectory of the same particle was plotted again for consistency. All the filtered x-and y-positions are saved in a new data structure, with the velocities that are analytically differentiated. Based on the velocities, the mean velocities are calculated, and a velocity profile for the fluidized suspension is plotted for x-and y-velocities alongside the horizontal axis. The velocities were initially obtained numerically using MATLAB's 'diff' built-in function. When both results were compared (see Figure 2.10), it is clear that the numerical solution filter out important peaks, especially near the wall region.

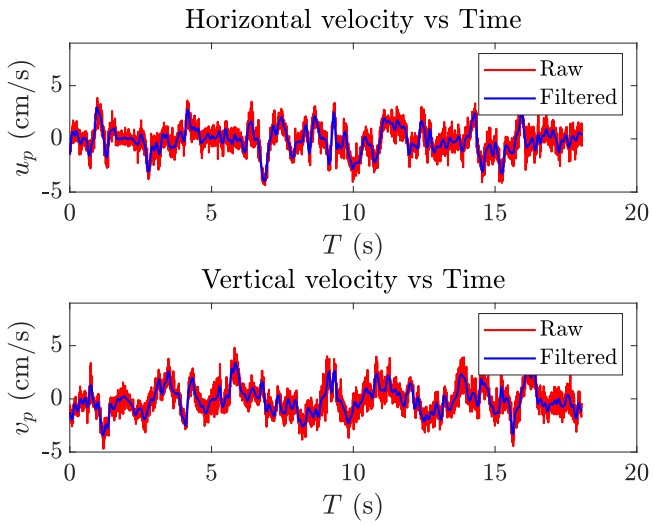

Figure 2.9: Filtered and unfiltered velocities over time of a single particle in the fluidized suspension.

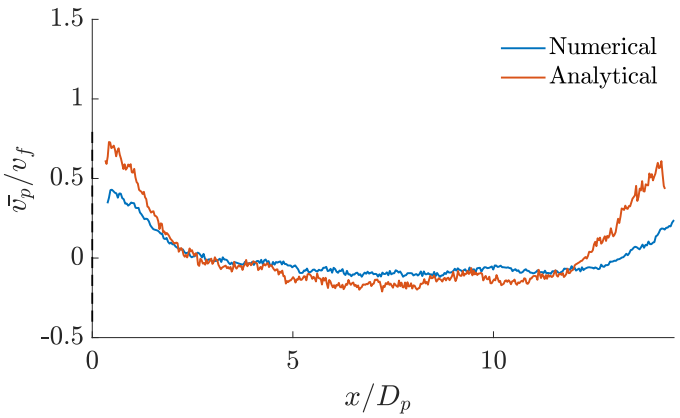

Figure 2.10: Mean vertical velocity profiles at Φ = 8% for Ga = 252. The analytical and numerical solutions are compared. The mean particle velocity is normalized with the fluidization velocity. The column's width is normalized with the particle diameter.

The velocity profile is calculated as follows. This includes finding the minimum and maximum x-positions across all particles, defining bin edges based on these, and initializing arrays to store the sum of velocities and count of particles for each bin. For each particle and for each time step, the

velocities are summed into the appropriate bin, and the particle count for that bin is incremented. The mean velocities for each bin are then calculated. Further analysis of the velocity profiles and interpretation of the results is discussed in Chapter 3 of this thesis. The velocity RMS profile is calculated in a similar fashion to the velocity profile but with squared velocities summed in each bin divided by the mean. The RMS velocities are then calculated as the square root of the averaged squared velocities and subtracted from the mean value from the velocity. The velocity profiles and the RMS velocity profiles are then plotted, showing how they vary along the column's width.

Further statistics can be obtained, such as plotting a PDF (probability density function) for the normalized velocities, instantaneous snapshots of the particles concentration over time, as well as particle conditional averaging. All the performed experiments and obtained results are discussed in Chapter 3.

2.6. Summary

In conclusion, the methodology chapter offers a detailed account of the experimental setup, procedures, and post-processing techniques. This starts with an in-depth exploration of the experimental procedures employed. The chapter highlights the experimental methodology, encompassing the design procedure, constraints, and experimental setup.

The experiments are done with PP spheres with water as the working liquid, having a liquid-solid density ratio fixed at 0.87. The Ga is from 147-255, and Φ is altered from 4-20%. The fluidization column is built with the sensors, and each one of those is clearly explained. The direct optical measurement methods used are also clearly discussed. Data logging is facilitated through a LabVIEW program, ensuring efficient and accurate data collection. The post-processing operations are a critical component of the methodology. The study employs a Savitzky-Golay filter to eliminate noise from the initial positions obtained for the velocity calculations. The filter parameters include a fourth-order polynomial and a frame length varying between 31-51 depending on the case. These were determined through an iterative process for each specific scenario. This filter was crucial in smoothing the position data and estimating velocities, paving the way for higher-order statistics calculations.

3

Results and Discussion

3.1. Experimental setup Validation

Before performing any experiment, the setup had to be validated with a single-phase flow. To achieve this, a moody diagram is obtained for the rectangular channel duct. A Moody diagram is a log-log plot displaying the relationship between the friction factor and the Reynolds number. The friction factor can be obtained either by using the Darcy-Weisbach equation (see Eqn. 1.15) or calculated analytically. To accurately measure the pressure drop, the following needs to be considered.

It is important to have a fully developed flow before running an experiment, therefore, the entrance length is a key parameter not to be overlooked. Additionally, it is important to stay below the transition flow regime. According to Hartnett [60], the critical Re for rectangular ducts with an aspect ratio of 10:1 is given as 4400. Darcy-Weisbach equation is used to calculate the friction factor based on the measured pressure drop and velocity. The pressure drop is measured between two consecutive pressure taps over a height difference of 10 cm. The flow rate varied between $0.1 - 2.0[L/min]$, resulting in single-phase Reynolds numbers ranging from approximately 100 to 1300. This range in Re did not reach the critical Reynolds number necessary for the turbulent regime.

Analytically solving for any cross-section is possible for the laminar flow velocity distribution, volume flow, and friction factor. This is accomplished by mapping any cross-section onto a circle using complex variables and using other analytical methods. While it is usually sufficient to use the hydraulic diameter to calculate a modified Reynolds number for laminar flow, incorporating the aspect ratio can result in even greater accuracy. This is especially pertinent because Reynolds stresses can cause secondary flow patterns in the corners, which are absent in laminar flow, and can significantly affect the results [61].

To find the friction factor analytically, different correlations have been developed for the friction factor in rectangular ducts [61, 62]. Among these, the correlation provided by White [63]. The basic friction factor correlation given is, $f = cRe^{-1}$, where c is 64 in a laminar region for a circular pipe. For rectangular ducts, we either had to use an effective diameter or extrapolate to adjust for the constant. The analytical solution took the form of $f = 89.9Re^{-1}$.

We then compared this empirical data with the analytical solution given by White et al. [63] in Figure 3.1. Reynolds number was calculated as follows $Re = UD_H/\nu_f$, where D_H is the hydraulic diameter of the rectangular duct. An uncertainty analysis was considered as well as the error bars. A linear axes scale is included in Figure D.1 in appendix D. These represent the uncertainties associated with our measurement equipment, as well as the standard deviations observed in our recorded data.

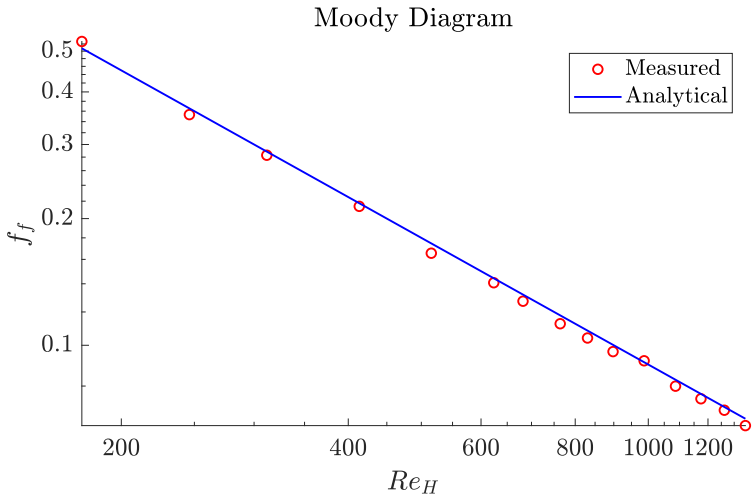

Figure 3.1: Moody Diagram fitted for the current experimental setup.

3.2. Single Rising Sphere

To understand the impact of confinement on the particle dynamics within our experimental setup, we used a high-speed camera to capture the motion of single rising spheres. This allowed us to calculate their terminal velocities. The procedure started by filling the system with water and a chiller is used to adjust the temperature to 20 °C. For these specific conditions, Ga is 196.23. We then mixed each PP sphere well with water using a tweezer before injecting it into the system at the lowest pressure tap with a syringe (see Figure 3.2). The camera was positioned to capture the particle's trajectory. After injection, each particle traveled 60 cm before reaching the field of view (21 cm). The images are captured at a rate of 50 fps.

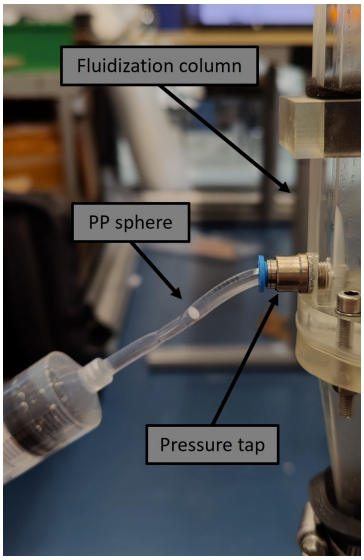

Figure 3.2: Syringe used for injecting the PP spheres into the system from the lowest pressure tap.

The raw positions of the sphere were obtained. Analytically differentiated, the filtered and unfiltered velocities were compared. It is essential to find the optimal polynomial order with the correct frame length as discussed in Chapter 2. There is an acceptable range in which the standard deviation of the velocities reaches a constant number. Beyond this range, the filter could distort the physical interpretation of the results. A 3rd-order Savitzky-Golay filter is applied with a frame length of 31.

The filtered velocities versus time were plotted to ensure each particle reached its terminal velocity. We repeated this experiment three times to ensure repeatability. There was a time interval of 5 minutes between each injection. This is necessary to ensure the liquid had returned to a state of stagnation and would not be affected by the previous experiment. For a bigger column, the time interval would vary between 15-30 minutes [64]. Given the consistency in the results, it is concluded that the disturbances in the fluid did not affect the terminal velocity.

This smoothed velocity profile provided a more realistic representation of the velocity field by reducing high-frequency noise that might have been introduced by uncertainties in our imaging technique. Figure 3.3 shows the terminal velocity plot, confirming that the particles indeed reached their terminal velocity.

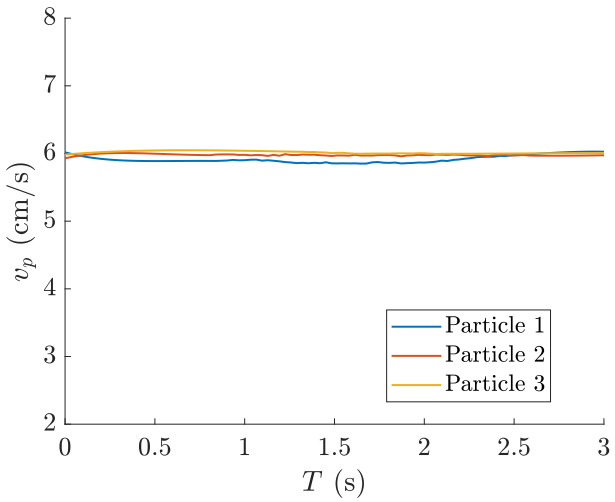

Figure 3.3: Filtered velocity vs time for single rising spheres experiments.

To calculate terminal velocity, we divided the displacement of the sphere in the x- and y- directions by the time interval. To verify that terminal velocity was achieved, we performed calculations as a function of time, confirming that the particles indeed reached their terminal velocity and were no longer accelerating. The k-factor, or wall effect factor, is determined by calculating the ratio between the terminal velocity of the sphere in an infinite medium and the terminal velocity in the confined medium. The k-factor is often used in R-Z correlations to predict the fluidization velocity and pressure drop. This ratio is expressed as $k = \frac{U_{t,\infty}}{U_p}$, where $U_{t,\infty}$ is the terminal velocity in an infinite medium calculated using Eqn. 1.11. U_p is the terminal velocity of the sphere measured in the confined medium. In our experiments, k was calculated to be 0.918.

3.3. Experimental Results

The preliminary experiments were conducted using water as the working fluid, with the help of an RP845 Lauda chiller. The bulk solid volume fraction was controlled by adjusting the volumetric flow rate or adding specific quantities of particles to the column. The Galileo number was controlled by modifying the working fluid's temperature.

The experiments primarily focused on three different Galileo numbers: $Ga = 147.11 \pm 3.28$, $Ga = 196.23 \pm 4.40$, and $Ga = 252.69 \pm 5.98$. The uncertainty in Ga was calculated as described in Appendix D. For each of these Ga values, the effect of inertia on various bulk solid volume fraction was analyzed. Φ was categorized into three key regimes: a dilute concentration regime up to 3%, a moderate concentration regime between 6% and 15%, and a dense concentration regime above 15%.

In the subsequent sections, we first examine the instantaneous spatial particle distribution across these regimes. Following that, we determine mean particle velocity profiles and calculate the particles' RMS velocities. The variations in RMS velocities with respect to the horizontal direction are taken into account. In addition, the probability density function (pdf) of normalized particle velocity is obtained for horizontal and vertical velocities, which provides a straightforward way to examine the suspension's microstructure. We also assess the extent of particle clustering and how it is influenced by changes in Ga and Φ.

3.3.1. Particle trajectories

For an initial inspection of the system, the trajectories of 2 different particles were plotted for the whole time frame. In dilute cases, it is clear that the spheres have the tendency of moving in the vertical direction, which is shown in Figure 3.4a. The particle motion fluctuations are strongly anisotropic, with vertical fluctuations much larger than horizontal fluctuations. While for the high-concentration regimes, the spheres tend to stay more in the horizontal direction. Figure 3.4b clearly shows the movement a single particle can exhibit during a fluidization experiment, which is the main reason the PTV algorithm was challenging. The plots also support that the data are sufficiently long in time to observe the long-time behavior of the spheres in the fluidized suspension.

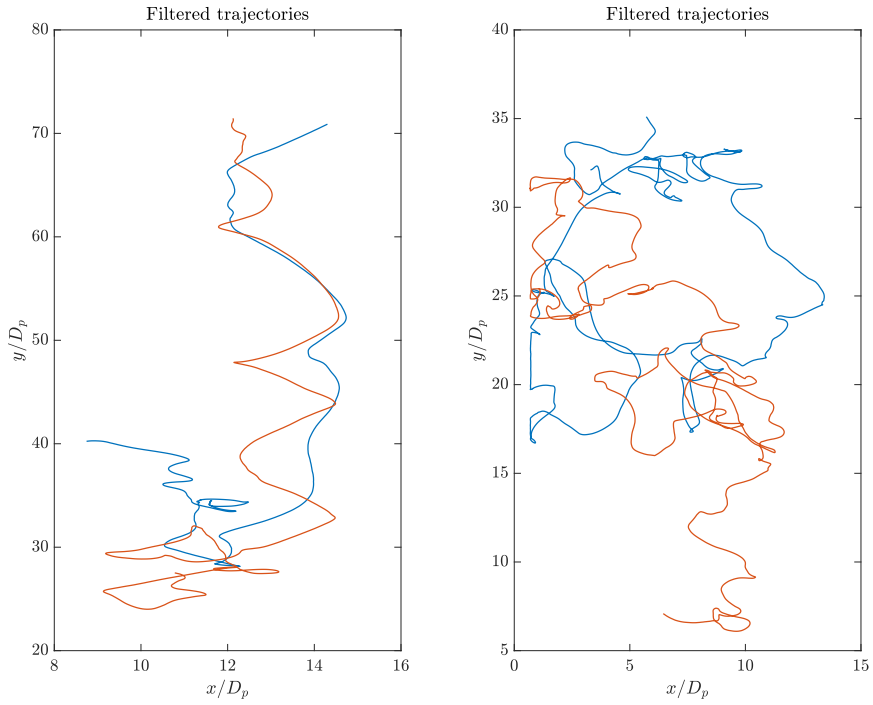

(a) **(b)**

Figure 3.4: Trajectories of two spheres in the fluidized suspension normalized by the particle's diameter at (a) dilute and (b) dense regime respectively.

3.3.2. Instantaneous spatial particle distribution

In this study, 2-D liquid-solid inverse fluidization experiments were executed to study the effect of inertia on the behavior of particles in a fluidized suspension. Instantaneous spatial particle distributions were generated and plotted to understand the movement of particles within the suspension.

Figure 3.5 displays the particle distribution for various Φ of 3%, 8%, 11%, and 16%, and Ga of 147, 196, and 252 respectively. Particles are color-coded according to their normalized vertical velocities relative to the superficial liquid velocity. For particles moving downward with a velocity higher than the normalized velocity, $v_p/v_f > 1.2$ are colored red. If these particles are close to the wall region, then they experience more drag than the average particle drag. This could be caused due to the intrinsic convection. However, if this happens in the middle, then the particles indicate the presence of some accelerated velocities due to clustering and possible DKT. Particles moving downward with normalized velocities close to unity ($0.5 < v_p/v_f < 1.2$) are colored orange. Other particles moving upward ($-0.5 > v_p/v_f > -1.2$) with a velocity close to the fluidization velocity are colored green. Slow particles that have a normalized velocity close to zero, $-0.5 > v_p/v_f$ and $v_p/v_f < 0.5$ are colored black. This indicates the particles are almost fully suspended, or that they are experiencing some hindered settling. Particles colored blue are going upwards with a relatively high velocity $v_p/v_f < -1.2$. The vertical clustering present in the core of the channel is proof of present intrinsic convection in these experiments.

The snapshots clearly show that in all cases a large number of particles are fluidized at different velocities. At dilute and intermediate regimes, the particles tend to move upwards in the core of the suspension, while particles with high velocities tend to be falling near the walls. This kind of circulation is further explained in the following sections when discussing the velocity profiles. At dense regimes, particles going in the upward direction seems to be moving more towards the walls, depending on the captured instant. Furthermore, the spheres going in the upward direction, mostly go in vertical columns consisting of doublets (i.e. DKT), triplets, and in some cases quadruplets. It was also noticed that while some spheres are going upwards, they tend to tumble beside each other, and then start falling again

in horizontal columns side by side. That was most prominent during the dilute regime.

For a sedimenting suspension with intrinsic convection, the particles should settle faster in the center of the cell than near the side walls. This difference is caused by the global convection of the suspension which is superimposed on the settling motion of the particles relative to the suspension [44]. There might be several reasons behind this circulation. Some particles exhibit locally strong return flow, which may drag them in a certain direction. There are also hydrodynamic particle interactions and particle bouncing after collisions that affect the particles moving near the walls. During the inverse fluidization experiments, the particles especially tend to go closer to the wall. When comparing figures 3.5a, 3.5b, and 3.5c, it shows that as Ga increases, more particles have a higher velocity in the core than that at lower Ga. Therefore, there is a higher probability of having clusters such as DKT at higher inertial regimes. However, this conclusion should be supported by additional quantitative analysis and statistical data. For experiments done at higher concentrations, particle ordering near the wall seems very important for explaining the reduced magnitude of the convection as would later be discussed in the velocity profiles.

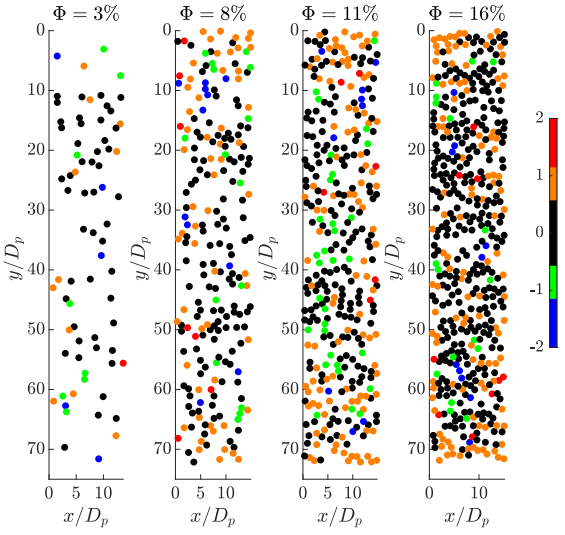

(a)

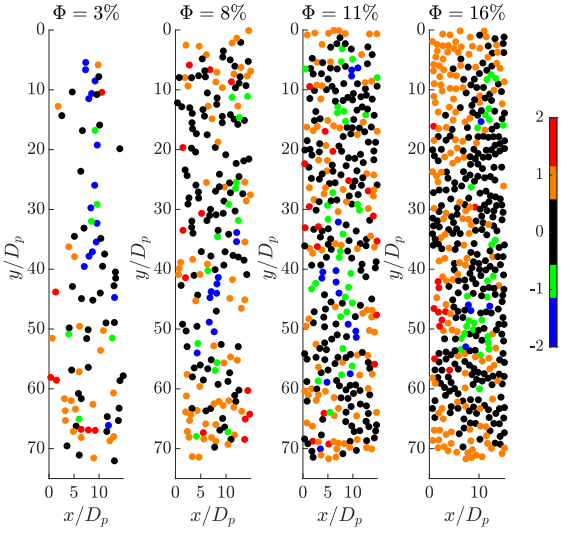

(b)

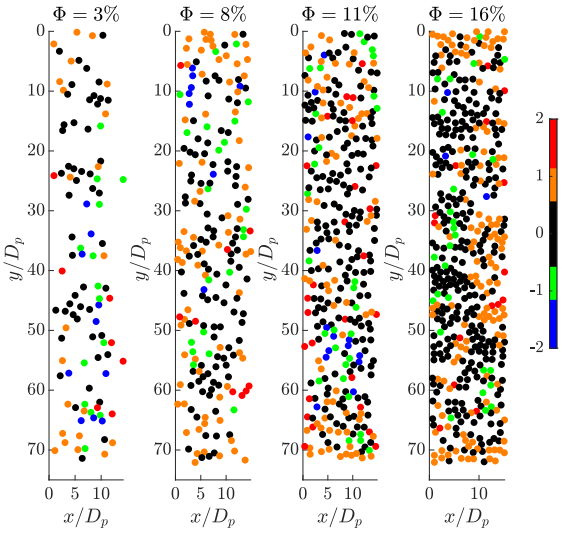

(c)

Figure 3.5: Instantaneous snapshots of the spatial particle distribution in the fluidized suspension as a function of Galileo number and bulk solid volume fraction. (3.5a) Ga =147.11, (3.5b) Ga = 196.23, (3.5c) Ga = 252.69. Note that blue is for upward moving particles ($v_p/v_f < -1.2$). Green is for particles moving upwards as well with a slower velocity ($-0.5 > v_p/v_f > 1.2$). Orange is the particles moving downwards ($0.5 < v_p/v_f < 1.2$). Red is for particles moving with a velocity higher than the normalized velocity ($v_p/v_f > 1.2$). Finally, black is for slow particles moving in both directions ($-0.5 > v_p/v_f$ and $v_p/v_f < 0.5$).

Ga = 147

Performing experiments at dilute regimes with $\Phi \approx 2\%$ were challenging. The minimum fluidization velocity at this concentration is very close to the terminal velocity of a single particle. The fluidization velocity is measured as 4.7, 5.3, and 5.7 cm/s for Ga of 147, 196, and 252 respectively. Once a particle is trapped in the wake of another particle, that reduces the drag experienced by the particle causing it to start falling down. At one point, the suspension is not homogeneous anymore and the whole suspension is flushed.

Ga = 196

To ensure the uniformity of the particle concentration throughout the experiments, Figure 3.6 was generated to depict the concentration as a function of time for a constant Ga and Φ. This figure confirms the stability of the bulk solid volume fraction throughout the experiment. For a clear visualization of the experiments done for a dilute regime, supplementary videos are added at Ga 147, 196, and 252, labelled red, blue, and black respectively. The movies are exported at a frame rate of 82 fps.

Overall, while the snapshots provide a preliminary understanding of particle behavior, further analysis, quantification, and statistical assessment are necessary to support the observations and uncover more comprehensive insights into the dynamics of the 2-D liquid-solid inverse fluidization system.
The following subsections discuss the velocity profiles and velocity RMS profiles for the fluidized suspension. This is beneficial for a more in-depth analysis of particle clustering and the effects of inertia in this confined geometry.

Ga = 252

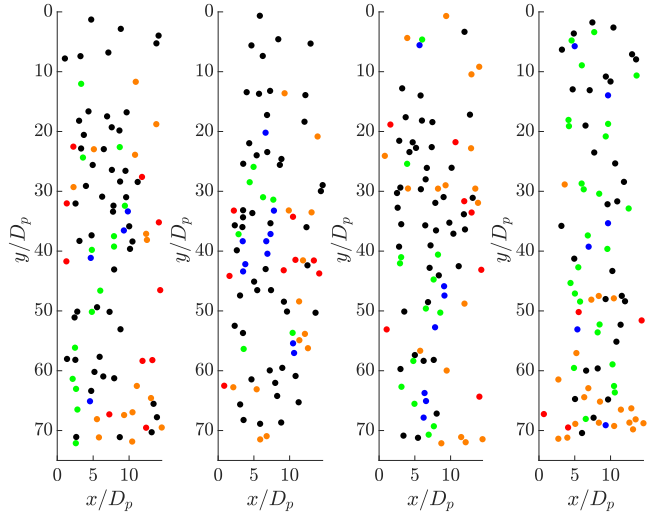

Figure 3.6: Instantaneous snapshots of the spatial particle distribution in the fluidized suspension at Ga = 197 and Φ = 3%. The figures have 92, 86, 88, and 84 particles in the field of view respectively.

3.3.3. Mean fluidization velocity

The mean velocity profile provides an understanding of the overall flow behavior within the suspension. It provides information about the velocity distribution across the cross-section of the system, revealing the velocity gradients and patterns such as intrinsic convection. By analyzing the mean velocity profile, regions of higher and lower velocities are identified. The flow direction and any asymmetries or non-uniformities in the suspension were also noted. For a clear discussion, the mean velocity profiles were divided into 3 categories, a dilute concentration regime ($\Phi = 3\%$), a moderate concentration regime ($\Phi = 11\%$), and a dense regime ($\Phi = 16\%$).

First, focusing on the dilute regime, Figure 3.7 was obtained at Ga =147, 196, and 252. The mean vertical velocity profile along the horizontal direction is normalized with the fluidization velocity. At the lowest Ga value, the significant influence of wall effects is observed up to a distance equivalent to $3x/D_p$ from both sides inside the channel. Lower Ga values correspond to lower inertia, resulting in a stronger impact of wall effects on the flow. With a lower particle concentration, the flow is particularly affected by the proximity to the walls. The noise present was also more prominent as lower Ga for the same

bulk solid volume fraction. At the lowest concentration with the lowest effect of inertia experienced in these experiments (Ga = 147), the intrinsic convection was not as prominent. As Ga value increases for the dilute regime, the velocity profile near the walls becomes more symmetric and the presence of the intrinsic convection is clear.

Ga = 147

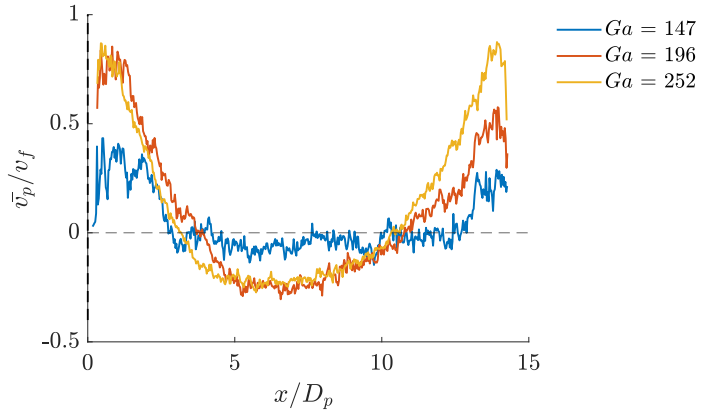

Figure 3.7: Mean vertical velocity profiles at Φ = 3% for various Ga. The mean particle velocity is normalized with the fluidization velocity. The x-axis is normalized with the particle's diameter. The black dashed horizontal line marks the value of $\overline{v_p}/v_f = 0$.

Ga = 196

Ga = 252

At the walls, the fluid has to obey a no-slip condition, so particles are less exposed to flow on average and hence tend to move downward. However, in the core, the particles will have to move upward as the net particle velocity for stable fluidization is zero. As mentioned in Chapter 1, this is related to intrinsic convection. If a full parabolic shape was present, that would indicate a laminar flow regime and suggests that the fluid is well-organized and follows predictable patterns. For the moderate regime, Figure 3.8 was obtained. At this bulk solid volume fraction, it is clear that the normalized mean vertical velocity profiles are consistent, regardless of increasing Ga. This suggests that increasing Ga in the inertial regime between 150-250 has minimal effect on these experiments. Across all three Ga values, a similar flow profile is observed with no significant distinctions. At Ga of 252, the slope of the mean velocity profile is steeper near the walls, which suggests the only influence Ga has on the fluidized suspension. Finally, for the experiments done at a moderate regime, supplementary movies corresponding to these experiments are added for Ga 147, 196, and 252 on the right side.

Ga = 147

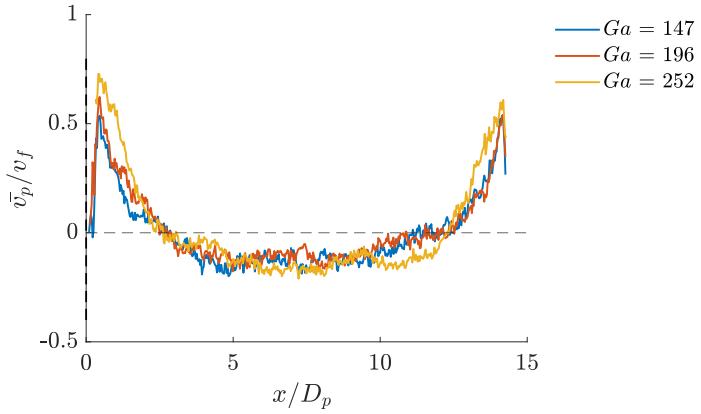

Figure 3.8: Mean vertical velocity profiles at Φ = 11% for various Ga. The mean particle velocity is normalized with the fluidization velocity. The x-axis is normalized with the particle's diameter. The black dashed horizontal line marks the value of $\overline{v_p}/v_f = 0$.

Ga = 196

Ga = 252

Focusing on the dense regime, Figure 3.9 is plotted. It is clear that the wall effects are damped, and has less effect on the mean velocity profile, unlike with lower concentrations. The presence of negative velocities suggests the presence of flow patterns and localized regions of fluid motion opposite to the bulk flow direction. Supplementary movies for experiments performed at a dense regime are added on the left for Ga 147, 196, and 252 respectively.

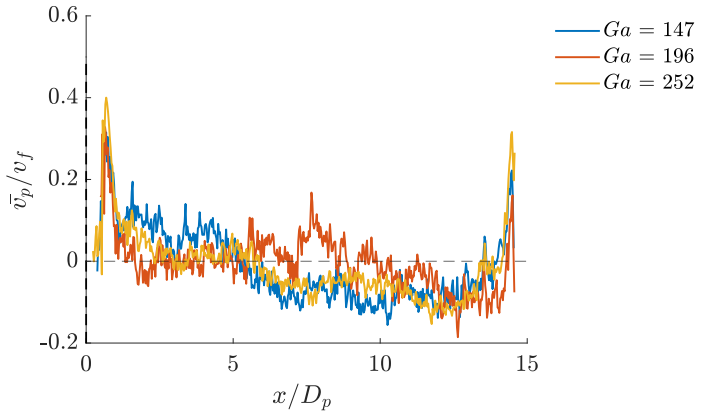

Figure 3.9: Mean vertical velocity profiles at Φ = 16% for various Ga. The mean particle velocity is normalized with the fluidization velocity. The x-axis is normalized with the particle's diameter. The black dashed horizontal line marks the value of $\overline{v_p}/v_f = 0$.

Having studied how the velocity profiles change with respect to Ga, it is beneficial to take a closer look on the effect of bulk solid volume fraction at a constant Ga. For a fixed Ga at 252, Figure 3.10 was obtained. The slight increase in velocity near the core for low concentrations indicates a subtle effect of particle interactions, while this effect is less pronounced for moderate concentrations. As Φ increases, the gradient of the parabolic shape in the velocity profile becomes less steep. This behavior can be attributed to the intensified fluid motion induced by higher interparticle interaction at the same Ga value. This causes more pronounced momentum transport, resulting in a sharper velocity gradient near the walls. At dense regimes, there are some asymmetries and non-uniformities in the velocity profiles. This might be caused due to intense collision between particles in the confined channel, as well as the particle-wall interactions that are happening.

The velocity profile varying with solid concentration suggests that the behavior of the suspension is influenced by the solid volume fraction of particles. These results were predicted by Bruneau's numerical model [43]. It was mentioned that the intrinsic convection decreases with increasing particle volume fraction. Peysson et al. [44] also concluded that increasing the volume fraction causes the amplitude of the intrinsic convection to diminish.

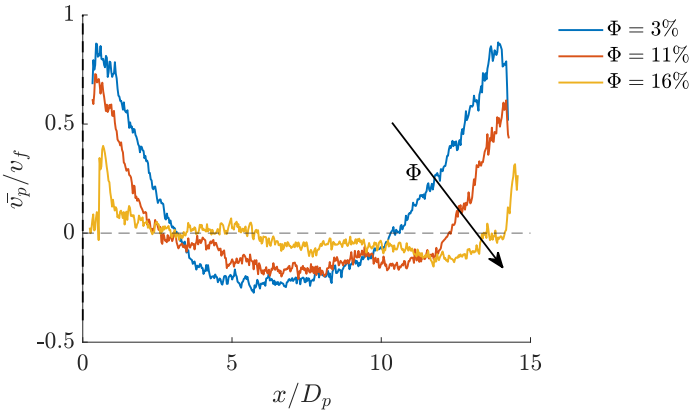

Figure 3.10: Mean vertical velocity profiles at $Ga = 252$ for various Φ. The mean particle velocity is normalized with the fluidization velocity. The x-axis is normalized with the particle's diameter. The black dashed horizontal line marks the value of $\overline{v_p}/v_f = 0$.

Overall, the described mean vertical velocity profile provides insights into the flow patterns and characteristics of the fluidized suspension. The intrinsic convection that was described in Figure 1.7 was obtained for a sedimenting suspension. It can be clearly observed in these experiments as well but in the opposite direction. This highlights the relevance of the wall effects. The confinement and the bulk solid volume fraction have an influence on velocity distribution and the presence of intrinsic convection in these experiments.

Regarding the mean horizontal velocity profiles, they exhibit a remarkable similarity across all cases as can be seen in Figure 3.11. The mean horizontal velocity is plotted across the column's width at a constant bulk solid volume fraction ($\Phi = 11\%$) for different Ga. Irrespective of implementing Savitzky-Golay (SG) filter, considerable noise and fluctuations were present. However, a consistent trend emerges. For a homogeneous fluidized bed, the vertical and lateral velocity has to be zero on the statistical average. This is due to mass conservation, otherwise, particles will accumulate in the system.

As a result, when further analyzing the results, and assessing the microstructure, it is important to focus on the core region of the column. The core region is taken with a distance of $2D_p$ from each side of the centerline. For the following sections, the mean RMS velocities are calculated for all the cases, as well as the velocity pdf. They are discussed for the total FOV, then focusing more on the core of the fluidization column.

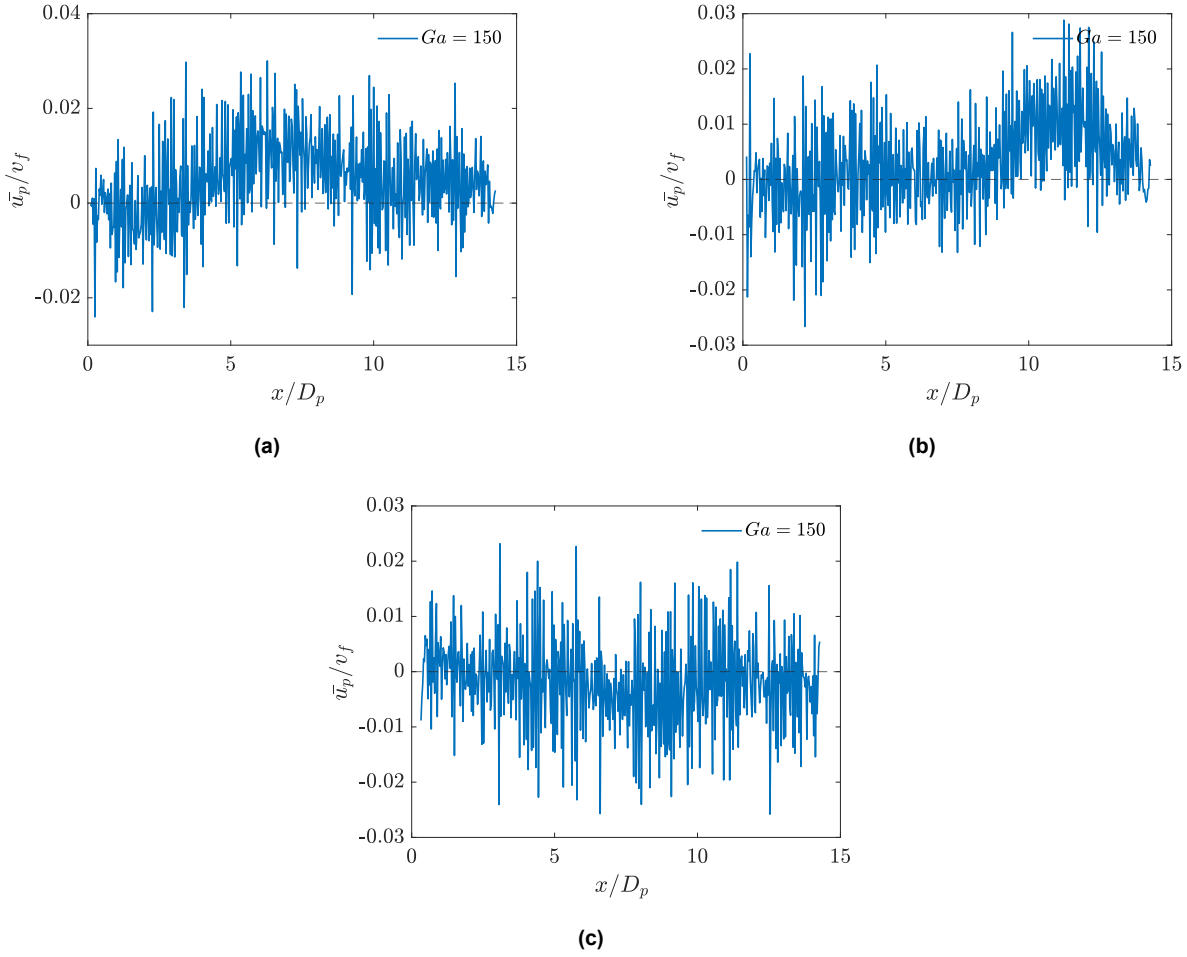

Figure 3.11: Mean horizontal velocity profiles for $\Phi = 11\%$. (a) Ga = 147. (b) Ga = 196. (c) Ga = 252. The mean particle lateral velocity is normalized with the fluidization velocity. The width of the column is normalized with the particle's diameter. The black dashed horizontal line marks the value of $\overline{u_p}/v_f = 0$

3.3.4. Mean RMS velocities

One of the objectives of this work is to measure the variation of the mean velocity as well as the velocity RMS across the column's width. The mean RMS velocities indicate the degree of relative motion between the particles and fluid.

The variations of the vertical particle velocity fluctuations are normalized by the fluidization velocity, with the horizontal position x/D_p presented in Figure 3.12 at $\Phi = 3\%$. Near the walls, increasing Ga leads to higher fluctuations. However, for the dilute regime, the system experiences the lowest normalized fluctuations at Ga of 147. As Ga increases, the fluctuations increase in the core compared to the sides, reaching a small peak in the middle of the fluidization column. At all Ga, it is observed that particles develop velocity fluctuations, which affects the average drag force. The higher RMS velocity in these regions might suggest stronger particle-particle interactions.

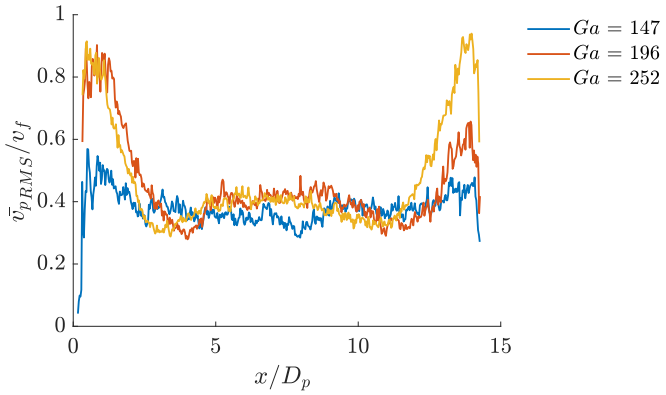

Figure 3.12: Mean RMS vertical velocity profiles at dilute regime, $\Phi = 3\%$. The RMS velocities are normalized with the fluidization velocity. The fluidization column's x-direction is normalized with the particle's diameter.

Further increasing the bulk solid volume fraction to a moderate regime at $\Phi = 11\%$, Figure 3.13 is plotted. All three Ga follow a very similar trend. With very high fluctuations near the walls, then slightly decreasing to reach a constant value in the middle regions. Even though Ga does not have a significant effect on the fluctuations, it is noticed as we increase Ga, the fluctuations decrease in the middle of the column. These positions correspond to locations where particles experience enhanced interactions. For higher local fluctuations, additional shear stress is produced in the fluid that increases the drag force.

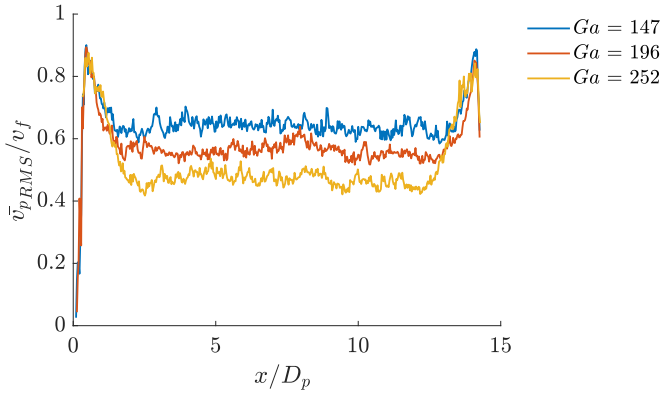

Figure 3.13: Mean RMS vertical velocity profiles at moderate regime, $\Phi = 11\%$. The RMS velocities are normalized with the fluidization velocity. The fluidization column's x-direction is normalized with the particle's diameter.

Finally, for the dense regime, Figure 3.14 is obtained. Similar to $\Phi = 11\%$, the highest fluctuations are present at the lowest Ga. As a general trend, both fluctuations seem approximately constant in the center of the cell and present a decrease near the side walls as previously noted. This behavior is observed even in the absence of intrinsic convection.

In all the cases mentioned above, the RMS velocity being zero at the walls indicates that the fluctuations in particle velocities are minimal in those regions. This is expected due to the no-slip condition. Particles in close proximity to the walls experience the highest drag, therefore have the highest fluctuations. The occurrence of a maximum RMS velocity is x/D_p of 2 and 13.

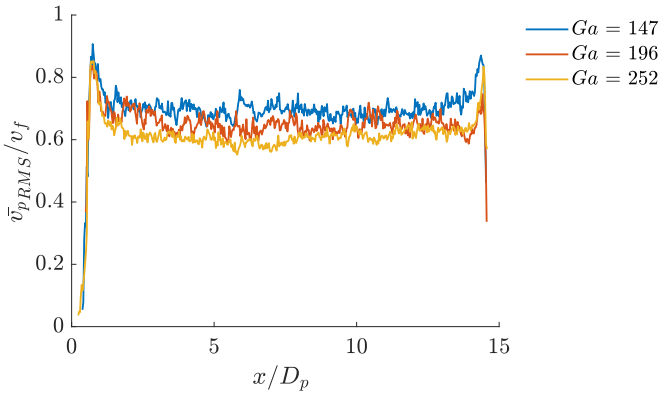

Figure 3.14: Mean RMS vertical velocity profiles at dense regime, $\Phi = 16\%$. The RMS velocities are normalized with the fluidization velocity. The fluidization column's x-direction is normalized with the particle's diameter.

To further study the effect of bulk solid volume fraction on the fluctuations, the mean RMS velocities are plotted at $Ga = 196$. Figure 3.15 shows that at the lower Φ, the velocity RMS differs in three different regions. Very close to the walls, then as we go closer to the centerline of the fluidization column, the fluctuations decrease and then increase again. However, at higher Φ, the difference is mainly between the wall and the core regions. Increasing Φ leads to higher fluctuations in the fluidized suspension. As was previously noted while studying the mean velocity profiles, the dynamics of the suspension is highly dependent on Φ.

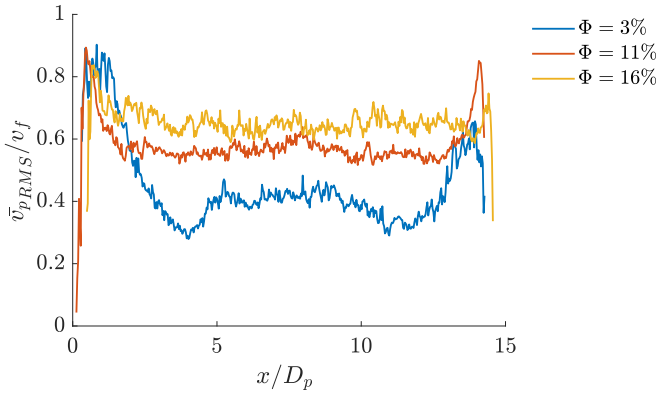

Figure 3.15: Mean RMS vertical velocity profiles at $Ga = 196$. The RMS velocities are normalized with the fluidization velocity. The fluidization column's x-direction is normalized with the particle's diameter.

Regarding the fluctuations in the lateral direction, Figure 3.16 is shown. For the dense regime, the normalized RMS velocity is plotted. In the fluidization experiments, the fluctuations in the lateral and vertical velocities are of the same order. A similar trend was observed for all other experiments. Increasing the Ga will cause a lower velocity RMS. This was expected given the plot obtained for the vertical velocity fluctuations.

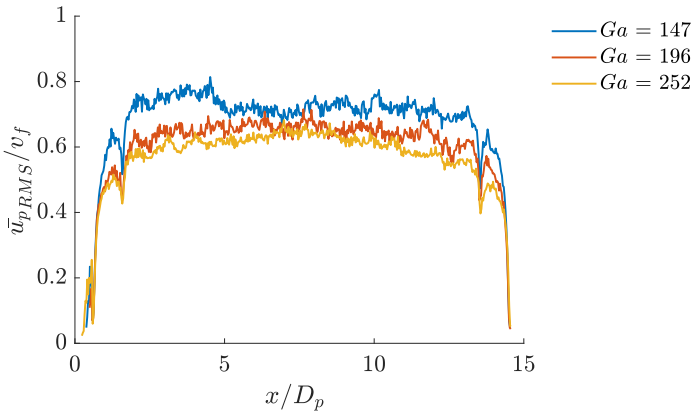

Figure 3.16: Mean RMS lateral velocity profiles at dense regime, $\Phi = 16\%$. The RMS velocities are normalized with the fluidization velocity. The fluidization column's x-direction is normalized with the particle's diameter.

In the region that is less affected by the side walls, a flat line is observed between 2 and 13 x/D_p, with a constant RMS velocity value. This indicates a relatively uniform level of velocity fluctuations within that region. This suggests that the particles in this region experience similar levels of interactions and cluster formation. The constant RMS velocity value indicates a consistent level of velocity fluctuations regardless of the distance from the wall.

To study the dependence of velocity fluctuations on the concentration of particles, a clear comparison of the velocity RMS at different regimes, Figure 3.17 was obtained while focusing on the core of the column. The core of the column is considered at the distance equal to $4D_p$. One can assume that in this area all the spheres are in similar hydrodynamic conditions as seen in the figures already obtained.

It is clear that as the bulk solid volume fraction increases, the fluctuations gradually decrease in both directions. The dependency of the RMS velocities on the bulk solid volume fraction is related to the short-range particle–particle interactions through lubrication and particle collisions. Most of the fluctuations in the core depend on the hydrodynamic interactions that might be related to clustering such as DKT-type instabilities.

The observed variation in the RMS velocity values with concentration indicates the influence of particle concentration on the intensity of velocity fluctuations. The higher velocity RMS at low concentration suggests more pronounced local turbulence and stronger particle-particle interactions. As the concentration increases, the RMS velocity decreases, indicating reduced turbulence and weaker fluctuations in particle velocities. This may be attributed to the increased presence of particles, leading to more crowded and constrained motion, resulting in dampened velocity fluctuations. Overall, the described RMS velocity profile provides insights into the intensity and distribution of velocity fluctuations within the fluidized suspension. It highlights regions of heightened particle interactions near the region of the wall.

The results are qualitatively in good agreement with the DNS results obtained by Shajahan et al. [30], especially at the moderately dense regime. Even though experiments were carried out at different Ga, they are at comparable regimes due to the influence of the wall. The fluctuations at Ga are qualitatively very similar, with the peaks present at Φ of 8%. However, for low Ga, the RMS in the horizontal direction is almost constant throughout all the different concentration regimes. For experiments done with higher levels of inertia, they exhibit a very similar trend. However, for Ga = 252, at the dilute regime,

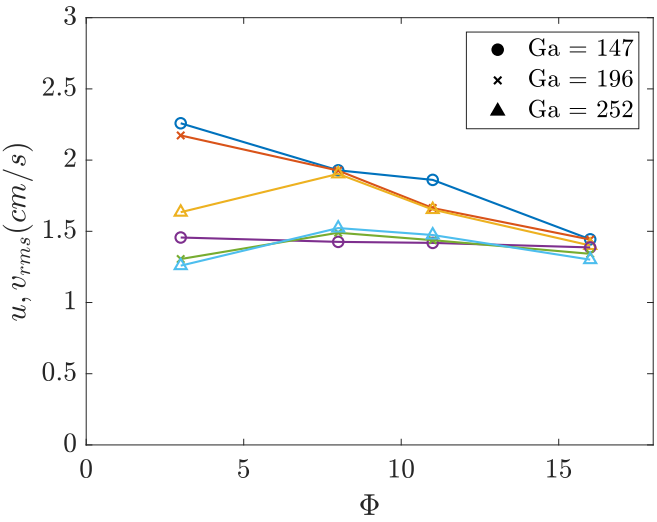

Figure 3.17: RMS velocity of particles as function of Ga and Φ focused on the core ($4D_p$). The upper 3 lines correspond to the vertical velocities. The lower 3 lines correspond to the lateral velocities. Circles, squares, and triangles correspond to Ga = 147, 196, and 252, respectively.

the RMS velocity in the vertical direction was the lowest. This would also support the conclusions made by Bruneau et al. [43] mentioning that non-random suspension microstructure, side-walls, or inertial screening may influence both random particle fluctuations and the mean fluidization velocity.

3.3.5. Pdf of particle velocity

To take a further step in understanding the microstructure of the fluidized suspension, the normalized probability density function (pdf) of the particle velocity in both directions is plotted. Figure 3.18 is obtained for the overall fluidization column. The normalized velocities are calculated by subtracting the mean velocity from each velocity and dividing by the RMS velocity. The plots are obtained as a function of Φ and Ga. Figures on the left, correspond to the lateral velocities while figures on the right are for the vertical velocities.

The pdf for the normalized lateral velocities primarily exhibits a super-Gaussian or Laplace-like distribution. Notably, this distribution deviates from the Gaussian norm by featuring a more pronounced peak and longer tails. This departure from the Gaussian model signifies an elevated occurrence of extreme velocities, implying that the system comprises particles with considerably high or low velocities.

Such a distribution, characterized by a marked positive kurtosis, is ascribed to the emergence of particle clusters in the system including DKT-type instabilities. The kurtosis is observed to be more pronounced in the dense concentration regime, suggesting that the formation of clusters increases under these conditions. In contrast, the pdf in the dilute regime embodies a less sharp peak, thus aligning more closely with the Gaussian model. An interesting deviation from this trend appears at the highest investigated Galileo number (see Figure 3.18e), corresponding to a combination between system dynamics and Ga.

Regarding the vertical velocity pdf, the results show a distinctive negative skewness. This trend intensifies with increasing Ga, indicating a tendency towards higher velocities. This could hint at the presence of wake trapping as well as columnar structures. However, this skewness seems unaffected by alterations in the bulk solid volume fraction when the walls are taken into account in the calculations. In a previous numerical study by Huisman et al., [29], the skewed pdf corresponded to the tendency of particles to form vertical columnar clusters. This is related to the inertial trapping of particles in the

wake of other particles.

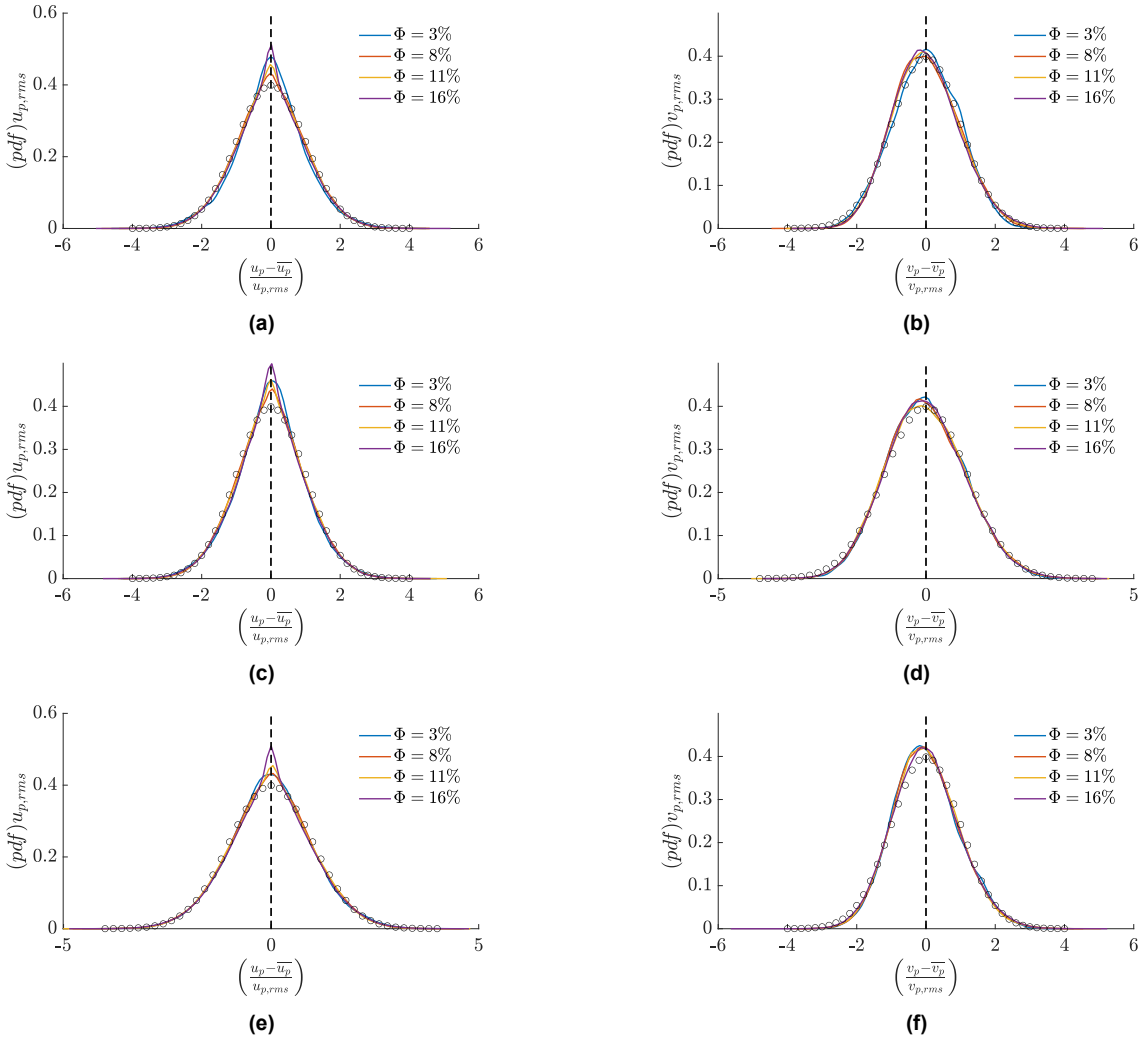

Figure 3.18: Probability density function of the lateral (u_p, left) and vertical ($v_p, right$) particle velocity as function of Φ and Ga (increasing from top to bottom). The pdf is normalized with the RMS particle velocity. Black circles represent a Gaussian distribution. (a) Lateral velocity, Ga = 147, (b) vertical velocity, Ga = 147, (c) lateral velocity, Ga = 196, (d) vertical velocity, Ga = 196, (e) lateral velocity, Ga = 252, (f) vertical velocity, Ga = 252.

Focusing more on the pdf in the core ($4D_p$) rather than including the side walls, Figure 3.19 is obtained. Surprisingly, a shift in the kurtosis, from the lateral to the vertical direction, becomes apparent when the core of the system is considered. Under dilute conditions, the core showcases a larger range of vertical velocities. At the lowest Ga, the pdf of the vertical velocity (Figure 3.19b) is similar for all of the various Φ and highest for the moderate regime. However, increasing the concentration causes the super-Gaussian distribution curve to be less prominent. For Ga of 196, and 252, Figures 3.19d and 3.19f are plotted respectively.

Both of these graphs exhibit consistent behavior. Going at a Ga beyond 196 did not change the behavior of the particles' movement. The highest positive kurtosis is noticed at the dilute regime and decreases as Φ increases. Even though the behavior of the velocities is closer to a Gaussian distribution, it never reaches a full Gaussian curve. At higher bulk solid volume fraction, the Gaussian distribution is consistent with a tendency towards a more random particle arrangement at all Ga. This is attributed to the dominance of short-range particle–particle interactions in particle dynamics.

For the pdf of the lateral velocities when focusing on the core ($4D_p$). Figure 3.19a shows positive skewness for the dilute regime at $Ga = 147$. Further increasing the concentration at the same Ga results in a collapse to a random Gaussian distribution. The collapse of the pdfs in the dense regime indicates that the velocity fluctuations scale with the RMS velocity. Even at a higher Ga, the velocity pdf shows similar behavior.

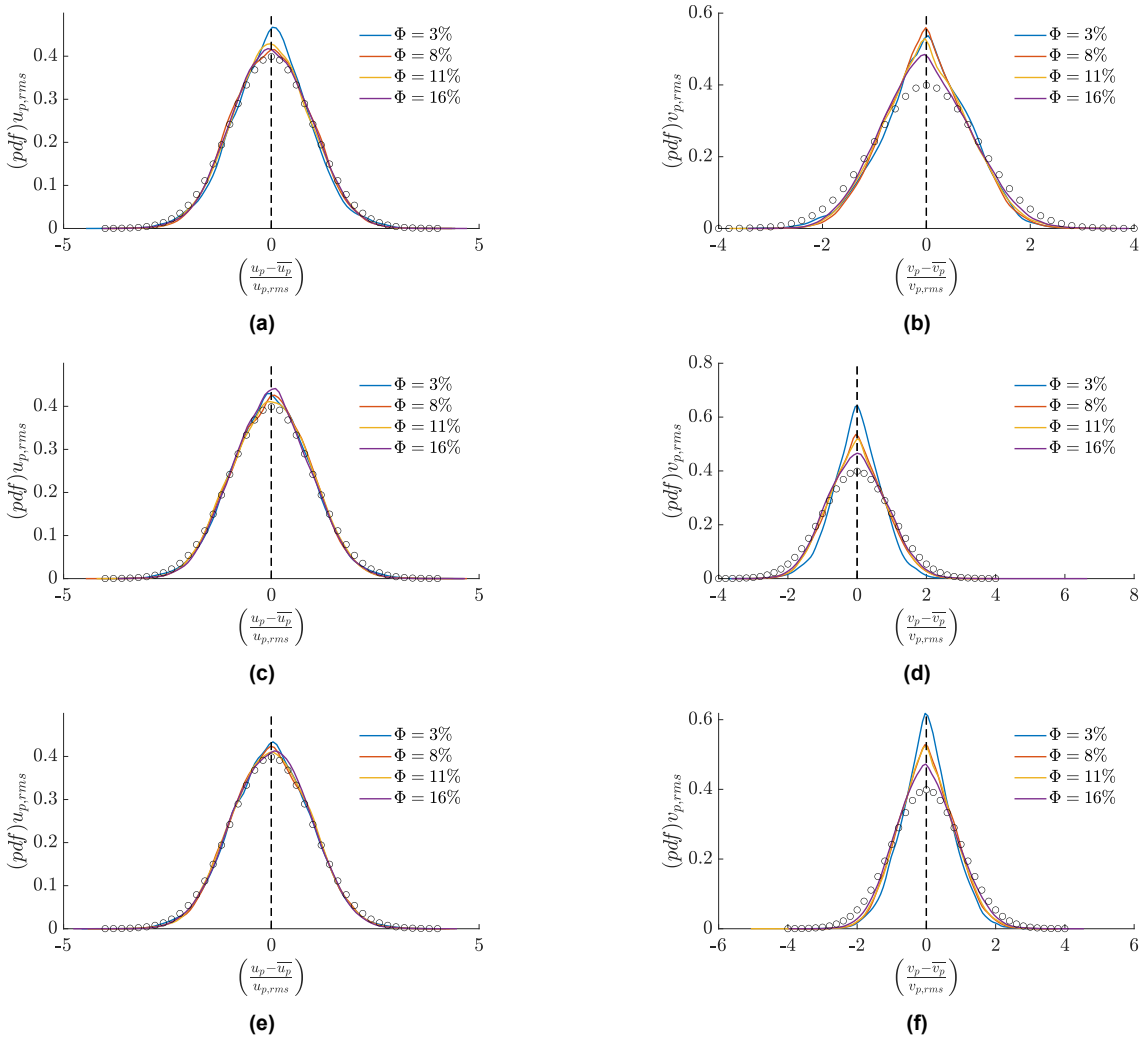

Figure 3.19: Probability density function focused on the core region ($4D_p$) of the fluidized suspension. The lateral (u_p, left) and vertical ($v_p, right$) particle velocity as function of Φ and Ga (increasing from top to bottom). The pdf is normalized with the RMS particle velocity. Black squares represent a Gaussian distribution. (a) Lateral velocity, Ga = 147, (b) vertical velocity, Ga = 147, (c) lateral velocity, Ga = 196, (d) vertical velocity, Ga = 196, (e) lateral velocity, Ga = 252, (f) vertical velocity, Ga = 252.

4

Conclusions

An experimental setup was designed and built to study the effect of inertia on liquid-solid fluidization. A high-speed camera is used to capture the particles. Subsequently, a PTV code is developed to track the mono-disperse spheres in a rectangular channel.

As concluded from Figure 1.8, there is a clear gap in the literature at a wide range of Ga and Φ. The effect of bulk solid volume fraction in the span of $\Phi = 4 - 18\%$ is studied. The study also focused on the effect of inertia, at various Ga of 147, 196, and 252. It is important to investigate the various effect on the suspension microstructure and its dynamics.

The trajectories of the spheres in the fluidized suspension were obtained. Higher-order statistics were calculated from the PTV data. These include the mean velocity profiles in the lateral and vertical directions. Furthermore, the RMS velocities were obtained, as well as the probability distribution function (pdf) of the lateral and vertical particle velocities. Based on the results obtained in Chapter 3, the role of inertia in inverse fluidization is studied.

For the experiments performed at various Φ, the fluidized suspension dynamics depend mostly on the solid volume fraction. For a specific Φ, the results are in a qualitative agreement for all Ga. The mean velocity profiles gave insights into the strength of the intrinsic convection present in the fluidization experiments. Intrinsic convection decreases with increasing Φ at a constant Ga. The wall effects are damped by increasing the particle volume fraction. This was mostly noticed by visualizing the mean vertical velocity profiles as a function of the column's width. Increasing Ga had no significant influence on the normalized mean velocity profiles plotted.

Calculating the particle mean RMS velocities give insight into the velocity fluctuations present in the suspension. Generally, both horizontal and vertical fluctuations are approximately constant in the center of the column. Close to the walls, they increase to local maxima and decrease again at the side walls. In the dense regime, this trend is observed whether or not intrinsic convection is present. Therefore, it does not seem to be tightly linked to the intrinsic convection phenomenon. The magnitude of the fluctuations seems to be affected primarily by the solid volume fraction. Although increasing the inertial effects play a role in particle clustering, it is evident that the volume fraction has a significant impact.

The pdf of the particle velocity sheds light on the effect of the inertial hydrodynamic interactions between particles. It was found that by increasing the solid volume fraction, a higher level of clustering happens. The calculations also proved the difference in particle dynamics present between the near-wall area and the core of the fluidization column, within $4D_p$ of the centerline.

The pdfs of the vertical particle velocities exhibit negative skewness, hinting at wake trapping and columnar structures. These are indicative of specific particle clustering. While the pdfs of the lateral particle velocities show a positive kurtosis and are characterized by a super-Gaussian distribution. This

is an implication of the system's tendency towards higher velocities and the presence of particle clusters.

Surprisingly, when focusing on the core of the fluidization column a shift in kurtosis from lateral to vertical direction is observed. Along with a tendency towards a more random particle arrangement at higher bulk solid volume fractions. The collapse of the pdfs in the dense regime indicates that the velocity fluctuations scale with the RMS velocity. These insights provide a valuable understanding of particle dynamics and interactions within the system.

As a result, particle clustering phenomena are attributed to multiple factors ranging from particle wake trapping to drafting–kissing–tumbling (DKT) instability. This showcases the complex interplay of forces and interactions within the system. Moreover, the prominence of wall effects and their dynamic response to changes in both Φ and Ga is shown.

5

Recommendations for future work

After performing thorough experiments in solid-liquid fluidization, this section is dedicated to the recommendations for future research. There are several points that would improve the understanding of microstructure formation in fluidization and sedimentation. The study of fluidization is characterized by four dimensionless numbers, D_p/L, Φ, $\overline{\rho}$, and Ga. In the following paragraph, the effect of each one of these is mentioned.

Initially, for the same experimental setup built, it is possible to conduct 3-D experiments by utilizing an MRI system with smaller particles. Performing these experiments would validate the results obtained from this research. This would also focus on hydrodynamic interactions happening away from the walls by having a smaller D_p/L.

Additionally, increasing the bulk solid volume fraction to the range of $\Phi = 30-40\%$ is recommended. Such a dense regime will provide an opportunity to observe the flow characteristics at higher concentrations, especially the damping of wall effects and the intrinsic convection. The magnitude of intrinsic convection is still far from being understood for 2-D experiments, as well as for 3-D experiments.

Experiments done in this research had a constant particle/fluid density ratio $\overline{\rho} = 0.87$. It would be interesting to study the effect of varying $\overline{\rho}$ at different Ga. The change in the wake and path trajectories might affect the overall suspension dynamics.

As was observed in the regime map obtained, there is still a gap in the literature, especially at lower Ga. It is important to explore the transition point at which inertial effects cease to be significant by systematically decreasing Ga. This investigation will yield valuable information about the dominance of inertial forces in the flow. This can be achieved by using a different working fluid (i.e. Aq. Glycerine).

The quantification of cluster size and a closer look at the microstructure formed in the fluidized suspension is important. This can be done by utilizing Particle Pair Distribution Functions (PPDF) or Radial Distribution Functions (RDF). The microstructure of the suspension can be accessed by means of the particle-conditioned average. This will provide a quantitative perspective on cluster formation, which is essential for interpreting particle-particle interactions.

Takeaways from the experiments:

1. Minimizing air bubbles: Eliminate air bubbles by utilizing the critical micelle concentration of Tween. Care should be taken not to overuse it, as an excess can lead to the formation of soap bubbles within the system.
2. Potential air leaks: Detect minor leakages that might introduce air into the system. A practical solution involves pressurizing the system to prevent air ingress, allowing controlled water leakage instead.
3. Valve handling and system filling: Exercise caution when manipulating valves and filling the system. Slow and deliberate filling procedures are recommended to prevent the attachment of air bubbles to the system's surfaces.
4. Precision in tilt angle adjustment: Ensure careful adjustment of tilt angles, recognizing their significant influence on results and inflow conditions. Accurate calibration of tilt angles is vital for maintaining experimental accuracy.
5. Precision building the fixed bed (liquid distributor) Carefully place the spherical particles in the fixed bed before the fluidization column. Having a fixed bed with a lower bulk solid volume fraction might enhance the inflow conditions by avoiding channeling.
6. Regular camera calibration: Calibrate the camera consistently each time the system is opened or closed. Even in cases where sole usage is anticipated, camera calibration is essential due to its sensitivity to changes over time.

A

Technical drawings

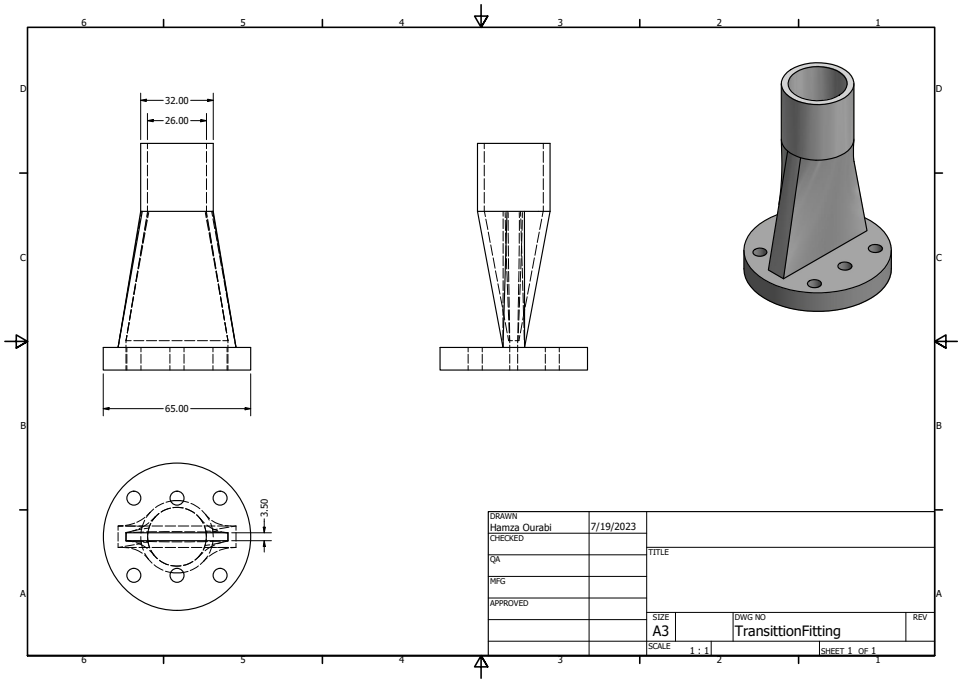

Figure A.1: CAD drawing of the duct-pipe transition fitting.

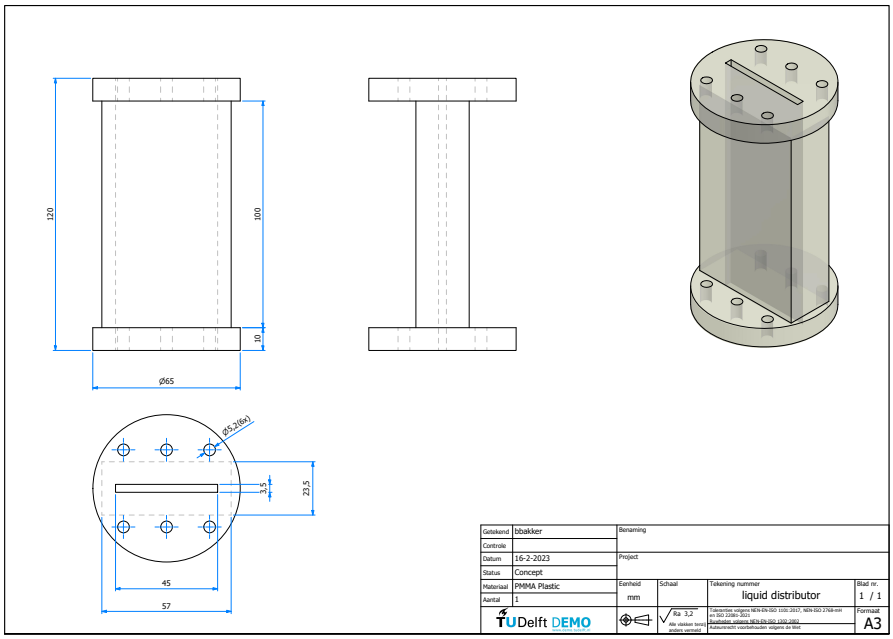

Figure A.2: CAD drawing of the liquid distributor.

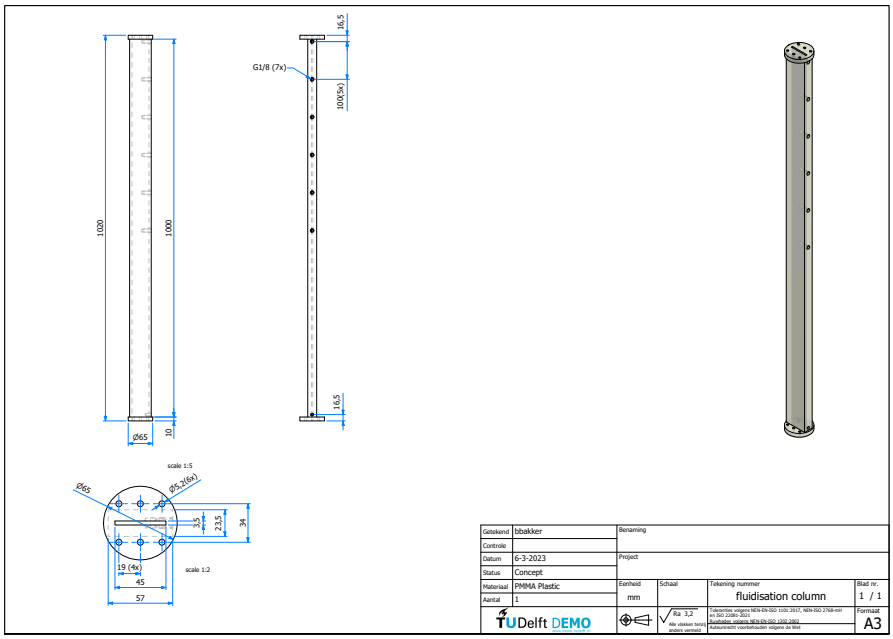

Figure A.3: CAD drawing of the fluidization column.

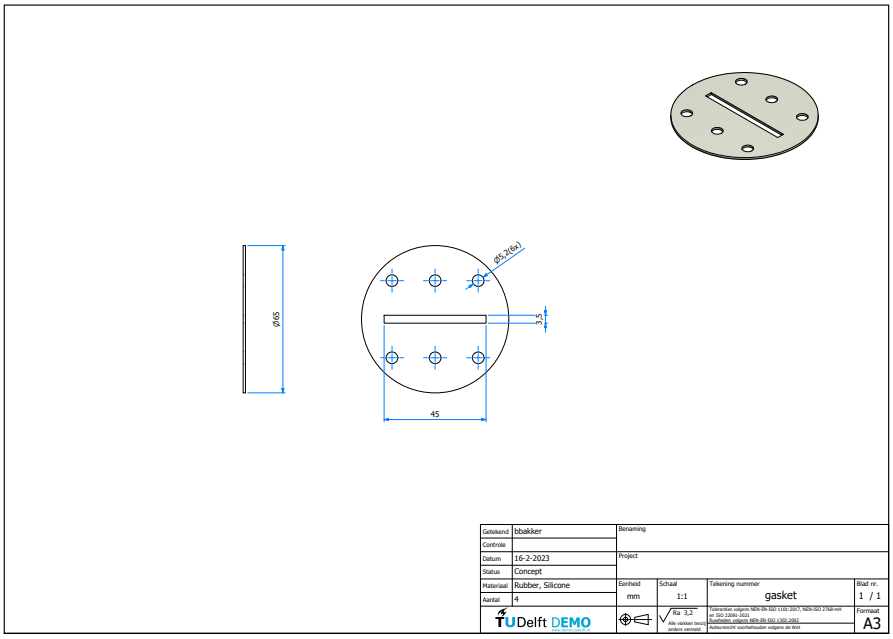

Figure A.4: Silicon metal gasket for water-tightness.

B

Calibration curves

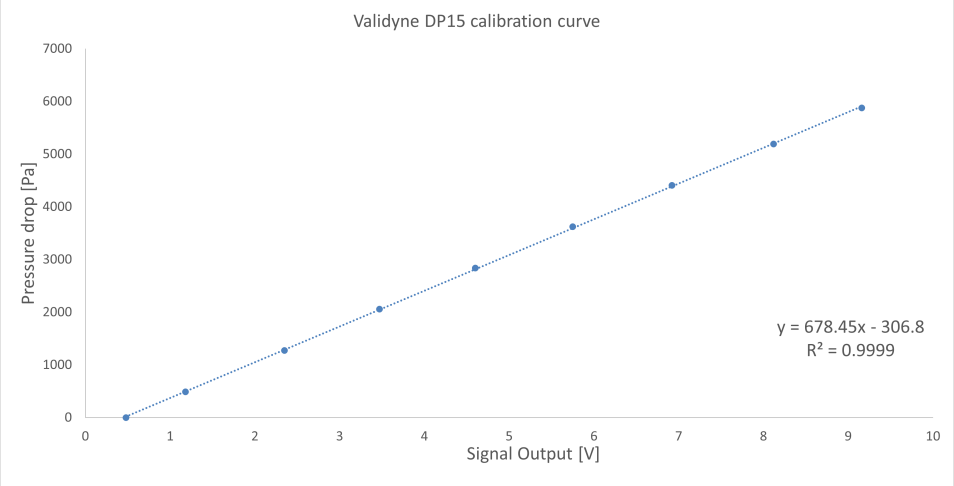

Figure B.1: Measured calibration curve fitted for Pressure drop vs Voltage output.

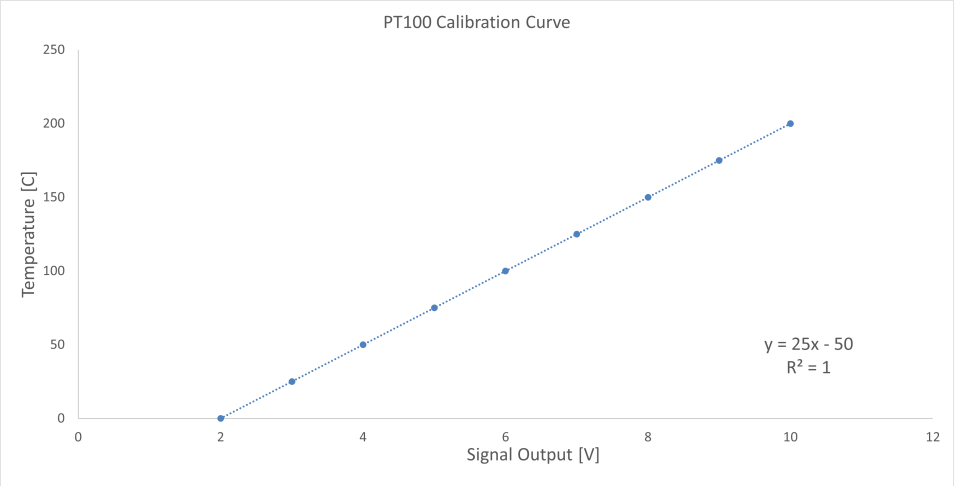

Figure B.2: Calibration curve fitted for Temperature vs Voltage output given by supplier.

C

Sphere measurements

To accurately measure the spheres diameter. First of all, the camera was constructed on a beam with a light source lying on the ground. The camera had a single focus lens, thus when the optimal distance was found, the camera was fixed. Later, using a calibration grid, a picture was taken to get a conversion factor from pixel to mm. Later, a batch of 50-60 spheres were placed in a petri dish. And the process was repeated for more than 50 times to obtain enough data for statistics. Once the pictures were obtained, they were imported to MATLAB. Using imfindcircles function, the position and radii of each sphere was found. Initially, it was manually done on several pictures to ensure no false diameters are being detected. Figure C.1 shows the process where the spheres were placed on the light source, followed by the figures exported from MATLAB that has the correct diameters detected. A total of 3000 particles were analyzed in this manner, and pertinent statistics such as standard deviation, mean, and error were computed.

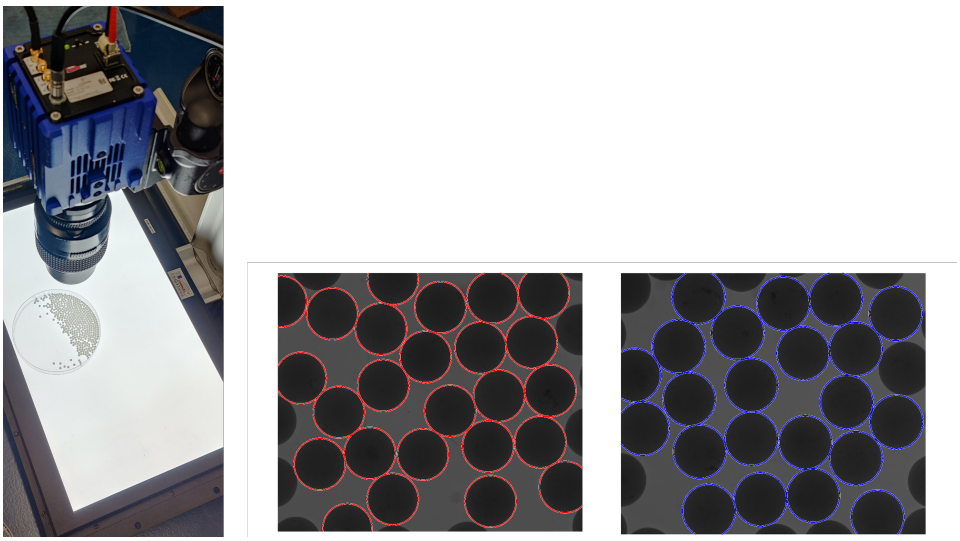

Figure C.1: Polypropylene spheres diameter measurement

After the measurements for the spheres diameter was done, it was important to obtain the weight of the spheres as mentioned in chapter 2. Using the scale shown in Figure C.2, accurate measurements were obtained for 12 particles at a time.

To match these density measurements, an extra step was taken to remove the outliers. As mentioned in chapter 2, the spheres were placed in Acetone, which has lower density than that of the spheres, to get a ballpark density. Using water/acetone mixture, different density liquids were prepared at 865, 870, 880, and 885 [kg/m^3]. The density of the spheres is set to fall within 870-880 [kg/m^3]. After the initial screening process, last mixture was made at 875 [kg/m^3], where the spheres were divided into 2 batches as can be seen in Figure C.3. A first batch having density 870-875 [kg/m^3], and

Figure C.2: Measuring the mass of 12 spheres

a second batch between 875-880 [kg/m^3]. The spheres were placed in a beaker, a PEG (Polyethylene Glycol) surfactant was used, and the spheres were left for 4-5 hours to settle. Most experiments were done on the first batch.

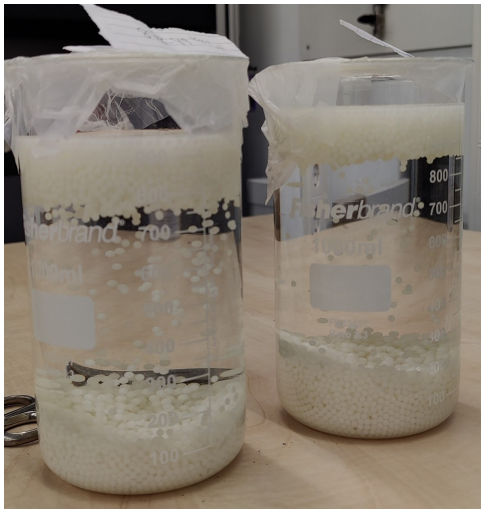

Figure C.3: Density match for PP spheres with Acetone

D

Uncertainty analysis

The Darcy-Weisbach friction factor f can be determined through the following equation:

$$f = \frac{2\Delta P d}{\rho u_b^2 L},$$

where f is the friction factor, ΔP is the pressure drop, d is the hydraulic diameter of the rectangular channel, ρ is the density of the fluid, u_b is the bulk velocity of the fluid, and L is the length of the channel.

The error in the friction factor δf due to the uncertainties in the pressure drop measurement $\delta(\Delta P)$ and the bulk velocity measurement $\delta(u_b)$ is given by the following error propagation formula:

$$\delta f = \sqrt{\left(\frac{\partial f}{\partial \Delta P}\delta(\Delta P)\right)^2 + \left(\frac{\partial f}{\partial u_b}\delta(u_b)\right)^2},$$

where

$$\frac{\partial f}{\partial \Delta P} = \frac{2d}{\rho u_b^2 L},$$

and

$$\frac{\partial f}{\partial u_b} = \frac{-4\Delta P d}{\rho u_b^3 L}.$$

Substituting the partial derivatives back into the error propagation formula:

$$\begin{aligned}\delta f &= \sqrt{\left(\frac{2d}{\rho u_b^2 L}\delta(\Delta P)\right)^2 + \left(\frac{-4\Delta P d}{\rho u_b^3 L}\delta(u_b)\right)^2} \\ &= \sqrt{\left(\frac{2d\delta(\Delta P)}{\rho u_b^2 L}\right)^2 + \left(\frac{4\Delta P d\delta(u_b)}{\rho u_b^3 L}\right)^2} \\ &= \frac{2d}{\rho u_b^2 L}\sqrt{\delta(\Delta P)^2 + \left(\frac{4\Delta P\delta(u_b)}{u_b^2}\right)^2}.\end{aligned}$$

This formula gives the uncertainty in the friction factor as a result of uncertainties in the pressure drop and bulk velocity measurements. In this propagation of errors, the errors arising from the hydraulic diameter and the length of the column were neglected. As the setup was precisely manufactured, these dimensions are constant and provided with high tolerance.

The Reynolds number, denoted by Re, is defined as:

$$\mathrm{Re} = \frac{\rho u_b d}{\mu}, \tag{D.1}$$

where Re is the Reynolds number, ρ is the density of the fluid, u_b is the bulk velocity of the fluid, d is the hydraulic diameter of the channel, and μ is the dynamic viscosity of the fluid.

The uncertainty in the Reynolds number, δRe, can be calculated using error propagation, considering the uncertainties in the bulk velocity, $\delta(u_b)$, and the dynamic viscosity, $\delta(\mu)$. The general error propagation formula for the uncertainty in the Reynolds number is:

$$\delta\mathrm{Re} = \sqrt{\left(\frac{\partial \mathrm{Re}}{\partial u_b}\delta(u_b)\right)^2 + \left(\frac{\partial \mathrm{Re}}{\partial \mu}\delta(\mu)\right)^2}. \tag{D.2}$$

Now, let's calculate the partial derivatives of the Reynolds number with respect to u_b and μ:

$$\frac{\partial \mathrm{Re}}{\partial u_b} = \frac{\rho d}{\mu}, \tag{D.3}$$

$$\frac{\partial \mathrm{Re}}{\partial \mu} = -\frac{\rho u_b d}{\mu^2}. \tag{D.4}$$

Substituting these partial derivatives back into the error propagation formula:

$$\delta\mathrm{Re} = \sqrt{\left(\frac{\rho d}{\mu}\delta(u_b)\right)^2 + \left(-\frac{\rho u_b d}{\mu^2}\delta(\mu)\right)^2}. \tag{D.5}$$

This formula provides the uncertainty in the Reynolds number as a result of the uncertainties in bulk velocity and dynamic viscosity measurements.

However, to avoid over complexity in adding error bars in both axes. For a first analysis, it is often sufficient to consider error bars for the dependent variable only (in this case, the friction factor).

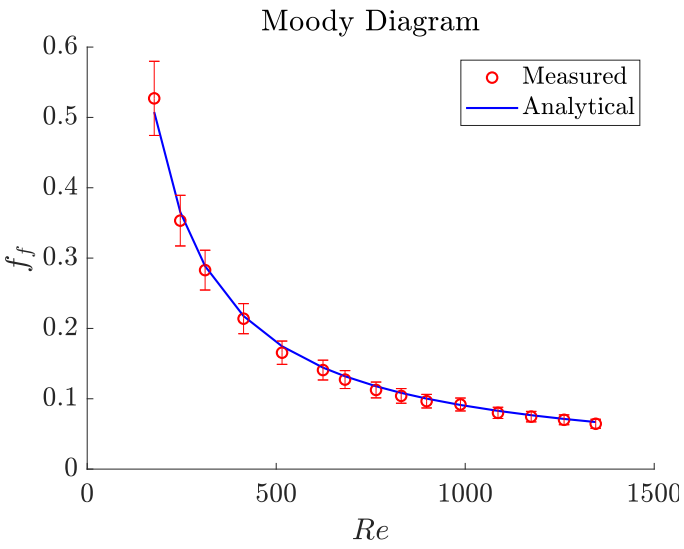

Figure D.1: Moody Diagram showing the error bars plotted.

For the Galileo number, it is also important to obtain a similar uncertainty analysis. The uncertainty in the Galileo number, $\delta(\mathrm{Ga})$, can be calculated using the error propagation formula:

$$Ga = \sqrt{\frac{m_p g - \frac{1}{6}\pi\rho_f g d_p^3}{\frac{1}{6}\pi\rho_f \nu_f^2}} \tag{D.6}$$

The estimate of uncertainty in Ga is given by the following expressions:

$$\delta Ga = \sqrt{\left(\frac{\partial Ga}{\partial m_p}\delta(m_p)\right)^2 + \left(\frac{\partial Ga}{\partial d_p}\delta(d_p)\right)^2 + \left(\frac{\partial Ga}{\partial \rho_f}\delta(\rho_f)\right)^2 + \left(\frac{\partial Ga}{\partial \nu_f}\delta(\nu_f)\right)^2} \tag{D.7}$$

Now, to access each of those, we have to calculate the partial derivatives in the above equation as follows,

$$\frac{\partial \mathrm{Ga}}{\partial m_p} = \frac{3g}{\pi\rho_f \nu_f^2 Ga}$$

$$\frac{\partial \mathrm{Ga}}{\partial d_p} = \frac{3g d_p^3}{2\nu_f^2 Ga}$$

$$\frac{\partial \mathrm{Ga}}{\partial \nu_f} = \frac{-Ga}{\nu_f}$$

$$\frac{\partial \mathrm{Ga}}{\partial \rho_f} = \frac{3m_p g}{\pi\nu_f^2 \rho_f^2 Ga}$$

These partial derivatives are substituted back into the equation for δGa to get the complete expression for the uncertainty propagation.

Bibliography

(1) Karamanev, D. G.; Nikolov, L. N. Bed expansion of liquid□solid inverse fluidization. *AIChE Journal* **1992**, *38*, 1916–1922.

(2) Kramer, O. J.; Padding, J. T.; van Vugt, W. H.; de Moel, P. J.; Baars, E. T.; Boek, E. S.; van der Hoek, J. P. Improvement of voidage prediction in liquid-solid fluidized beds by inclusion of the Froude number in effective drag relations. *International Journal of Multiphase Flow* **2020**, *127*, 103261.

(3) Cocco, R.; Karri, S. B.; Knowlton, T. Introduction to fluidization. *Chemical Engineering Progress* **2014**, *110*, 21–29.

(4) Harrison, D. Fluidization. **1974**, *61*, 191–217.

(5) Di Felice, R. The sedimentation velocity of dilute suspensions of nearly monosized spheres. *International Journal of Multiphase Flow* **1999**, *25*, 559–574.

(6) Woodruff, D., *Treatment of coal tailings*; Woodhead Publishing Limited: 2013, pp 529–559.

(7) Narayanan, C. M. Performance and applications of semifluidized bioreactors - A review. *International Journal of Chemical Reactor Engineering* **2019**, *17*, 1–19.

(8) Dong, Y.; Liu, C.; Wei, H.; Meng, Q.; Zhou, H. Size segregation mechanism of reclamation fill sand due to rainbowing operations in hydraulic dredging activities. *Ocean Engineering* **2021**, *242*, 109957.

(9) Raaghav, S. K.; Poelma, C.; Breugem, W. P. Path instabilities of a freely rising or falling sphere. *International Journal of Multiphase Flow* **2022**, *153*, 104111.

(10) F., R. J. Incipient Fluidization and Particulate Systems. *Fluidization* **1971**, *2*.

(11) Ergun, S. Fluid flow through packed columns. *Chemical Engineering Progress* **1952**, *48*, 89.

(12) Yin, X.; Koch, D. L. Hindered settling velocity and microstructure in suspensions of solid spheres with moderate Reynolds numbers. *Physics of Fluids* **2007**, *19*, 093302.

(13) Maron, S. H.; Pierce, P. E. Application of ree-eyring generalized flow theory to suspensions of spherical particles. *Journal of Colloid Science* **1956**, *11*, 80–95.

(14) Stokes, G. G. On the Effect of the Internal Friction of Fluids on the Motion of Pendulums. *Mathematical and Physical Papers* **2010**, 1–10.

(15) Coe, K.; Clevenger, G. Methods for Determining the Capacities of Slime-thickening Tanks. *Trans. AIME* **1916**, 203–210.

(16) Robinson, B. C. S. Some Factors Influencing Sedimentation. *Industrial and Engineering Chemistry* **1926**, *58*, 869–871.

(17) Di Felice, R.; Parodi, E. Wall Effects on the Sedimentation Velocity of Suspensions in Viscous Flow. *AIChE Journal* **1996**, *42*, 927–931.

(18) Arsenijević, Z. L.; Grbavčić, Ž. B.; Garić-Grulović, R. V.; Bošković-Vragolović, N. M. Wall effects on the velocities of a single sphere settling in a stagnant and counter-current fluid and rising in a co-current fluid. *Powder Technology* **2010**, *203*, 237–242.

(19) Shajahan, T.; Breugem, W. P. Influence of Concentration on Sedimentation of a Dense Suspension in a Viscous Fluid. *Flow, Turbulence and Combustion* **2020**, *105*, 537–554.

(20) Jenny, M.; Dušek, J.; Bouchet, G. Instabilities and transition of a sphere falling or ascending freely in a Newtonian fluid. *Journal of Fluid Mechanics* **2004**, *508*, 201–239.

(21) Clift, R.; Grace, J.; Weber, M., *Bubbles, Drops and Particles.* 2005.

(22) Richardson, J. F.; Zaki, W. N. Sedimentation and fluidisation: Part I. *Chemical Engineering Research and Design* **1997**, *75*, S82–S100.

(23) Wilhelm, R. H. Fluidization of Solid Particles. *Chem. Eng. Prog.* **1948**, *44*, 201–218.

(24) Kaye, B.; Boardman, R., *Cluster formation in dilute suspensions*, 1962, pp 17–21.

(25) Fortes, A. F.; Joseph, D. D.; Lundgren, T. S. Nonlinear mechanics of fluidization of beds of spherical particles, 1987.

(26) Jayaweera, K.; Mason, B.; Slack, G. The behaviour of clusters of spheres falling in a viscous fluid Part 1. Experiment. *Journal of Fluid Mechanics* **1964**, *20*, 129–139.

(27) Kajishima, T.; Takiguchi, S. Interaction between particle clusters and particle-induced turbulence. *International Journal of Heat and Fluid Flow* **2002**, *23*, 639–646.

(28) Uhlmann, M.; Doychev, T. Sedimentation of a dilute suspension of rigid spheres at intermediate Galileo numbers: The effect of clustering upon the particle motion. *Journal of Fluid Mechanics* **2014**, *752*, 310–348.

(29) Huisman, S. G.; Barois, T.; Bourgoin, M.; Chouippe, A.; Doychev, T.; Huck, P.; Morales, C. E.; Uhlmann, M.; Volk, R. Columnar structure formation of a dilute suspension of settling spherical particles in a quiescent fluid. *Physical Review Fluids* **2016**, *1*, 1–11.

(30) Shajahan, T.; Breugem, W. P. Inertial effects in sedimenting suspensions of solid spheres in a liquid. *International Journal of Multiphase Flow* **2023**, *166*, 104498.

(31) Liu, Y.; Yu, X. General formulation of drag force on assemblage of spherical particles in fluids: A critical review and a new empirical formula. *Physics of Fluids* **2022**, *34*, 063307.

(32) Reddy, R. K.; Sathe, M. J.; Joshi, J. B.; Nandakumar, K.; Evans, G. M. Recent developments in experimental (PIV) and numerical (DNS) investigation of solid-liquid fluidized beds. *Chemical Engineering Science* **2013**, *92*, 1–12.

(33) Yao, Y.; Criddle, C. S.; Fringer, O. B. The effects of particle clustering on hindered settling in high-concentration particle suspensions. *Journal of Fluid Mechanics* **2021**, *920*, 1–24.

(34) Nikolov, L.; Karamanev, D.; Zhelyazkov, T. Extended study on the hydrodynamics of a cold model of the inverse fluidized bed bioreactor. *Biotechnology and Biotechnological Equipment* **1994**, *8*, 75–79.

(35) Renganathan, T.; Krishnaiah, K. Voidage characteristics and prediction of bed expansion in liquid-solid inverse fluidized bed. *Chemical Engineering Science* **2005**, *60*, 2545–2555.

(36) Femin Bendict, R. J.; Kumaresan, G.; Velan, M. Bed expansion and pressure drop studies in a liquid-solid inverse fluidised bed reactor. *Bioprocess Engineering* **1998**, *19*, 137–142.

(37) Ulaganathan, N.; Krishnaiah, K. Hydrodynamic characteristics of two-phase inverse fluidized bed. *Bioprocess Engineering* **1995**, *15*, 159–164.

(38) Fan, L. S.; Muroyama, K.; Chern, S. H. Hydrodynamic characteristics of inverse fluidization in liquid-solid and gas-liquid-solid systems. *The Chemical Engineering Journal* **1981**, *24*, 143–150.

(39) Nikolov, L.; Karamanev, D. Experimental study of the inverse fluidized bed biofilm reactor. *The Canadian Journal of Chemical Engineering* **1987**, *65*, 214–217.

(40) Renganathan, T.; Krishnaiah, K. Prediction of minimum fluidization velocity in two and three phase inverse fluidized beds. *Canadian Journal of Chemical Engineering* **2003**, *81*, 853–860.

(41) Guazzelli, E.; Morris, J. F., *A physical introduction to suspension dynamics*; Cambridge University Press: 2011, p 139.

(42) Snabre, P.; Mills, P. Settling and fluidization of non Brownian hard spheres in a viscous liquid. *The European Physical Journal E* **2000**, *114*, 105–114.

(43) Bruneau, D.; Feuillebois, F.; Blawzdziewicz, J.; Anthore, R. Three-dimensional intrinsic convection in dilute and dense dispersions of settling spheres. *Physics of Fluids* **1998**, *10*, 55–59.

(44) Peysson, Y.; Guazzelli, E. An experimental investigation of the intrinsic convection in a sedimenting suspension. *Physics of Fluids* **1998**, *10*, 44–54.

(45) Volpicelli, G. Nonhomogeneities in solid-liquid fluidization. *Chem. Eng. Prog. Symp. Ser.* **1966**, *62*, 42–50.

(46) Miyamura, A. Experimental Wall Correction Factors and Square Cylinders , and Parallel Plates. **1981**, *7*, 41–46.

(47) Chhabra, R. P. Wall effects on free-settling velocity of non-spherical particles in viscous media in cylindrical tubes. *Powder Technology* **1995**, *85*, 83–90.

(48) Yao, S.; Chang, C.; Hai, K.; Huang, H.; Li, H. Journal of Petroleum Science and Engineering A review of experimental studies on the proppant settling in hydraulic fractures. *Journal of Petroleum Science and Engineering* **2022**, *208*, 109211.

(49) Brenner, M. P. Screening mechanisms in sedimentation. *Physics of Fluids* **1999**, *11*, 754–772.

(50) Garslde, J.; Al-Dibouni, M. R. Velocity-Voidage Relationships for Fluidization and Sedimentation in Solid-Liquid Systems. *Industrial and Engineering Chemistry Process Design and Development* **1977**, *16*, 206–214.

(51) Zhu, Z.; Zhou, M.; Yu, B.; Song, X.; Li, G.; Zhu, S.; Xu, Z.; Yao, X.; Liu, Z. Journal of Petroleum Science and Engineering A unified equation of settling velocity for particles settling in cylinder , annulus and fracture. *Journal of Petroleum Science and Engineering* **2022**, *213*, 110446.

(52) Dewsbury, K. H.; Tzounakos, A.; Karamanev, D. G.; Margaritis, A. Wall effects for the free rise of solid spheres in moderately viscous liquids. *Canadian Journal of Chemical Engineering* **2002**, *80*, 974–978.

(53) Abraham, F. F. Functional Dependence of Drag Coefficient of a Sphere on. **1970**, *2195*, 2194–2195.

(54) Chen, Y. M.; Jang, C. S.; Cai, P.; Fan, L. S. On the formation and disintegration of particle clusters in a liquid-solid transport bed. *Chemical Engineering Science* **1991**, *46*, 2253–2268.

(55) Rouyer, F.; Martin, J.; Salin, D. Non-gaussian dynamics in quasi-2D noncolloidal suspensions. *Physical Review Letters* **1999**, *83*, 1058–1061.

(56) Pan, T. W.; Joseph, D. D.; Bai, R.; Glowinski, R.; Sarin, V. Fluidization of 1204 spheres: Simulation and experiment. *Journal of Fluid Mechanics* **2002**, *451*, 169–191.

(57) An, X.; Liu, M.; Fu, Y. Clustering behavior of solid particles in two-dimensional liquid-solid fluidized-beds. *China Particuology* **2007**, *5*, 305–311.

(58) Jiang, Q.; Brunet, Y.; Kanit, T. Microstructure of the solid phase in fluidized beds for non-Stokes regimes. *European Journal of Mechanics, B/Fluids* **2010**, *29*, 435–441.

(59) Savitzky, A.; Golay, M. J. E. Smoothing and Differentiation of Data by Simplified Least Squares Procedures. *Analytical Chemistry* **1964**, *36*, 1627–1639.

(60) Hartnett, J. P.; Koh, J. C.; McComas, S. T. A comparison of predicted and measured friction factors for turbulent flow through rectangular ducts. *Journal of Heat Transfer* **1962**, *84*, 82–88.

(61) Jones, O. C. Improvement in the Calculation of Turbulent Friction in Rectangular Ducts. *Journal of Fluid Mechanics* **1976**, 173–180.

(62) Dean, R. Reynolds Number Dependence of Skin Friction and Other Bulk Flow Variables in Two-Dimensional Rectangular Duct Flow. *Journal of Fluids Engineering* **1978**, *100*, 215–223.

(63) White, F. M., *Fluid Mechanics 8th Edition*; 3, 2017; Vol. 11, pp 287–301.

(64) Toupoint, C.; Ern, P.; Roig, V. Kinematics and wake of freely falling cylinders at moderate Reynolds numbers. *Journal of Fluid Mechanics* **2019**, *866*, 82–111.